

Atlas 2 - Foundation models for clinical deployment

Maximilian Alber ^{* ‡ 1 13}, Timo Milbich ^{* 1}, Alexandra Carpen-Amarie ^{* 1},
 Stephan Tietz ^{# 1}, Jonas Dippel ^{# 1 7 8}, Lukas Muttenthaler ^{# 1 15 16},
 Beatriz Perez Cancer ^{# 1}, Alessandro Benetti ^{# 1}, Panos Korfiatis ^{# 3},
 Elias Eulig ¹, Jérôme Lüscher ¹, Jiasen Wu ¹, Sayed Abid Hashimi ¹,
 Gabriel Dernbach ^{1 8 13}, Simon Schallenberg ¹³, Neelay Shah ¹,
 Moritz Krügener ¹, Aniruddh Jammoria ¹, Jake Matras ⁵, Patrick Duffy ⁶,
 Matt Redlon ⁴, Philipp Jurmeister ^{11 12}, David Horst ^{11 13}, Lukas Ruff ¹,
 Klaus-Robert Müller^{† 7 8 9 10}, Frederick Klauschen^{† 8 11 12 13 14}, Andrew Norgan^{† 2}

¹ Aignostics, Germany

² Department of Laboratory Medicine and Pathology, Mayo Clinic, Rochester, MN, US

³ Department of Radiology, Mayo Clinic, Rochester MN, US

⁴ Department of Information Technology, Mayo Clinic, Rochester MN, US

⁵ Mayo Clinic, Rochester MN, US

⁶ Digital Pathology, Mayo Clinic, Rochester MN, US

⁷ Machine Learning Group, Technische Universität Berlin, Germany

⁸ BIFOLD – Berlin Institute for the Foundations of Learning and Data, Germany

⁹ Department of Artificial Intelligence, Korea University, Republic of Korea

¹⁰ Max-Planck Institute for Informatics, Germany

¹¹ German Cancer Research Center (DKFZ) & German Cancer Consortium (DKTK),
 Berlin & Munich Partner Sites, Germany

¹² Institute of Pathology, Ludwig-Maximilians-Universität München, Germany

¹³ Institute of Pathology, Charité – Universitätsmedizin Berlin, Germany

¹⁴ Bavarian Cancer Research Center (BZKF), Germany

¹⁵ Helmholtz Munich, Germany

¹⁶ Technical University Munich, Germany

^{*,#,†} Equal contribution respectively

[‡] Corresponding author

Abstract

Pathology foundation models substantially advanced the possibilities in computational pathology — yet tradeoffs in terms of performance, robustness, and computational requirements remained, which limited their clinical deployment. In this report, we present Atlas 2, Atlas 2-B, and Atlas 2-S, three pathology vision foundation models which bridge these shortcomings by showing state-of-the-art performance in prediction performance, robustness, and resource efficiency in a comprehensive evaluation across eighty public benchmarks. Our models were trained on the largest pathology foundation model dataset to date comprising 5.5 million histopathology whole slide images, collected from three medical institutions Charité - Universitätsmedizin Berlin, LMU Munich, and Mayo Clinic.

1 Introduction

Digital and computational pathology including large-scale slide digitization, virtual microscopy for diagnostics, and artificial intelligence (AI)-based histological image analysis have started to

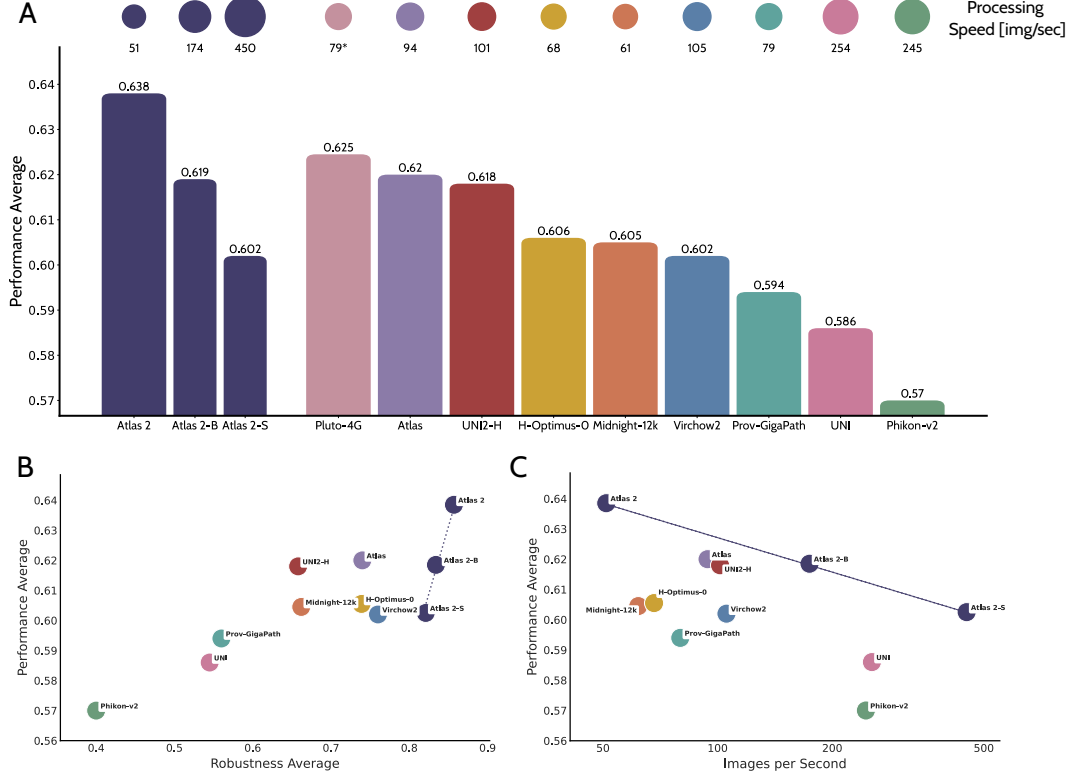


Figure 1: **(A)** The results show that Atlas 2 is the best performing model. Additionally Atlas 2-B and 2-S have similar prediction performance as contenders but are up to a magnitude more efficient. The performance average is based on morphology prediction tasks from *eva* [27] and molecular prediction tasks from HEST [34] in Table 1. The dots show the processing speed of the respective model for a 224×224 pixel image on an L4 GPU. The value for Pluto-4G [60] is approximated by taking the fastest speed of same sized models [38, 67, 79]. **(B)** The results show that Atlas 2, Atlas 2-B, and Atlas 2-S are the most robust models and also the state of the art performance-robustness Pareto front. The plot shows the performance average from (A) and the robustness average from Table 1. **(C)** The data shows that the Atlas 2 models are the performance-resource efficiency Pareto front. The plot shows the performance average of (A).

transform anatomic pathology and led to promising proof-of-concepts and applications [e.g., 45, 15, 65, 7, 44]. However, generalization and robustness remain challenging and have hindered the broad translation of AI applications into clinical routine diagnostics. Despite increasing digitization efforts, scarcity of training data, particularly for infrequent and rare diseases [18], remains a challenge. Furthermore, generating sufficient labeled data representing the full spectrum of human disease, biological, and technical variability inherent to morphology, tissue processing, staining, and scanners has proven logistically and financially challenging. Addressing these problems, pathology foundation models have recently gained traction based on their promise to achieve robust and generalizable data representations by incorporating the diversity present in pathology through large-scale self-supervised training. However, tradeoffs in terms of performance, robustness, and computational requirements remained and have so far limited their clinical impact. In this report, we present an updated version of our previously published pathology foundation model Atlas [2] that addresses these deficiencies. To this end, we substantially expand the underlying database by using a multi-centric corpus of 5.5 million histopathology whole slide images derived from Charité - Universitätsmedizin Berlin, LMU Munich, and Mayo Clinic, increase the model parameter count, and improve our training recipe to develop a novel pathology foundation model “Atlas 2”. We distill our main model into the lightweight versions “Atlas 2-B”, and “Atlas 2-S”, which are based on the more resource efficient architectures ViT-B and ViT-S. They can process a standard-size image 3.4 and 9 times faster, respectively. All models incorporate a broad diversity of diseases, staining types, and scanners, and utilize multiple image magnifications during training. We compare the performance of Atlas 2 to other leading models available for testing using eighty benchmarks assessing a variety of downstream pathology tasks. An overview of model characteristics and main results can be found in Figure 1 and Figure 2.

2 Related Work

Pathology foundation models In the past years pathology foundation models [17, 2, 82, 25, 79, 67, 13, 16, 60, 50, 35, 52, 64] established themselves as the basis for developing clinical-grade applications [77] in digital pathology. These models are divided into tile- or slide-based models. Tile-based models [17, 2, 82, 13, 8, 60, 39, 38] are trained via self-supervised-learning frameworks such as DINOv2 [59] or DINOv3 [69] to encode small, fixed-sized image tiles into compact embeddings. These embeddings then typically serve as a starting point to train slide-based pathology foundation models [52, 68, 77] which learn to aggregate the per-tile information into a single representation for an entire whole slide image (WSI) using slide-level supervision such as patient report- [52, 76, 68, 71] or molecular [73, 80] data. Key drivers of the success story of pathology foundation models are increasing both the number of WSIs powering foundation model training [2, 8, 82] and the capacity of such models by means of their encoder size [82, 8, 38]. The presented model Atlas 2 is the largest tile-based pathology foundation model to date with a total of 5.5 million WSIs being used to train a 2 billion parameter Vision Transformer [19].

Robustness of pathology foundation models While pathology foundation models are trained on increasingly large and diverse pretraining datasets, their lack of robustness to scanner, lab processing artifacts, and staining variations was observed to be still problematic [48, 22, 14, 46, 29, 51, 11, 12, 54]. This can lead to a substantial decrease in performance when prediction labels are correlated with such confounding information in the representations [49, 43, 48]. Multiple investigations have analyzed these shortcomings and proposed benchmarks to measure the robustness in this regard [22, 48]. So far, only limited work has been performed in improving the robustness of pathology foundation models. Examples are stain normalization [53, 66], data augmentation [20], projecting out confounder information [57, 48], distillation [22], or applying methods during downstream training (e.g. DANN [26, 48]).

Efficient pathology foundation models for clinical deployment To provide efficient alternatives to large-scale frontier pathology foundation models, several groups [82, 60, 23] have released lightweight counterparts by either training small encoders directly from scratch [60, 37, 55, 1] or performing knowledge distillation [31, 6] from larger foundation models [23, 82].

3 Data and Methods

3.1 Dataset and Preprocessing

We curate a dataset of 5.5 million de-identified WSIs, derived from the digital archives of Charité - Universitätsmedizin Berlin, LMU Munich, and Mayo Clinic, from which we extract tiles at multiple resolutions, namely 0.25, 0.5, 1.0, and 2.0 microns per pixel, corresponding to objective microscopic magnifications of 40 \times , 20 \times , 10 \times , and 5 \times , respectively.

3.2 Model Framework and Compute Environment

We perform model training in several phases. All of our model architectures are based on the Vision Transformer (ViT) [19], using a patch-token size of 8. For our main model, Atlas 2, we use a 2 billion parameter variant. For the distilled versions, Atlas 2-B and Atlas 2-S, we use the model sizes “base” (ViT-B; 86 million parameters) and “small” (ViT-S; 22 million parameters), respectively. Our training framework uses an adapted RudolfV [17] and Atlas [2] approach as well as novel developments. Parts of the framework are based on DinoV2 [59] and selective improvements from DinoV3 [69]. For model training, we use Nvidia B200 GPUs and Nvidia A100 GPUs.

3.3 Evaluation Protocols

For reproducibility and comparability, publicly available frameworks were used for the evaluation: HEST [34], eva [27], PathoROB [48], Plismbench [22] and Patho-Bench [81], covering tile-level as well as slide-level tasks. To further extend the pool of tasks, we additionally report a number of results for public benchmarks based on an in-house evaluation framework. To evaluate the quality of the foundation model embeddings, we keep the model encoders frozen and solely apply task-specific

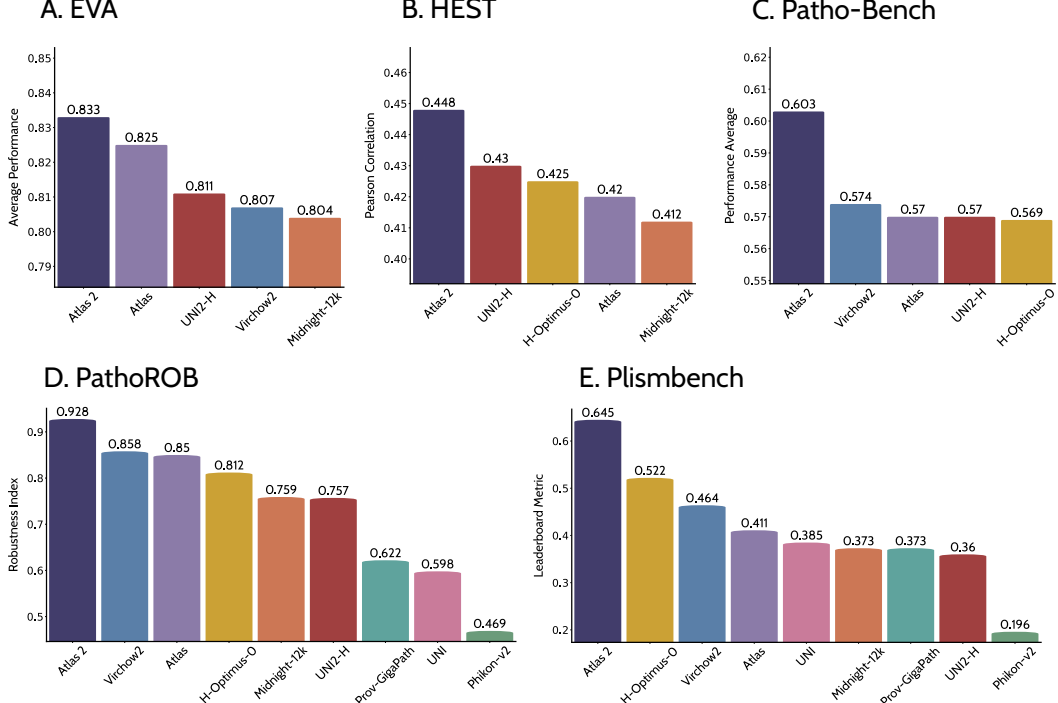


Figure 2: (A) - (E) show the average performance per evaluation framework [27], [34], [81], [48], and [22]. Atlas 2 is the leading contender on all frameworks.

prediction heads. Unless stated otherwise, we report results based on a concatenation of the CLS token and the mean over patch tokens (“CLS+MEAN”). Results for the CLS token can be found in Appendix A.2. Input images are normalized using the specified normalization statistics of the respective models. We do not apply normalization to the output tokens unless it is specifically done by the evaluation framework.

We evaluate 15 foundation models using their publicly available weights: UNI2-H [13], H-Optimus-0 [67], Midnight-12k [38], Virchow2 [82], Prov-GigaPath [79], UNI [13], Phikon-v2 [25], the ViT-B/8, ViT-B/16, ViT-S/8, and ViT-S/16 from [1], Hibou-B [56], Phikon [24], and the ViT-S/8, and ViT-S/16 from [37]. For five additional models, Pluto-4G [60], Pluto-4S-8 [60], Pluto-4S-16 [60], H-Optimus-1 [8], and H0-mini [22] we include comparisons based on published results, as model weights are either not publicly released or not accessible to us for evaluation.

HEST The HEST-Benchmark [34] is composed of tasks for gene expression prediction and designed as multivariate regression. We use the default evaluation protocol and implementation [30]. The protocol leverages a Ridge Regression with Principal Component Analysis (PCA) to solve the multivariate regression on the extracted foundation model embeddings. The results are based on the Pearson correlation coefficient as defined in [34]. Dataset details can be found in Appendix A.1.

eva The *eva* framework [27] comprises tasks for clinical prediction across various cancer types and pathology applications. Again, we use the default evaluation protocol and implementation [21]. For patch-level classification tasks, a linear classification head is trained on the CLS or CLS+MEAN tokens. For patch-level segmentation tasks, segmentation is performed on the extracted patch token embeddings. For slide-level classification tasks, *eva* applies the default Attention-based Multiple Instance Learning (ABMIL) [32] protocol. We use balanced accuracy as a performance metric for all patch-level and slide-level classification tasks. For patch-level segmentation tasks, Dice score without background is reported. Evaluation results are presented using the test split when provided, and the validation split when a test split is unavailable. Datasets details can be found in Appendix A.1.

PathoROB The PathoROB Robustness Index benchmark [48] is designed to evaluate model robustness with respect to non-biological, confounding features. We use their default evaluation

protocol and implementation [62]. Our average values for Virchow2 and Prov-Gigapath differ slightly from official values due to using bicubic image resizing instead of bilinear. This does not affect the ranking. We provide dataset details in Appendix A.1.

Plismbench The Plismbench benchmark [22] measures the representation consistency across different scanning and staining conditions. We use the default evaluation protocol and implementation [63]. We report the leaderboard metric, defined as the average of four metrics: cosine similarity for all pairs, top-10 accuracy for cross-scanner pairs, top-10 accuracy for cross-staining pairs, and top-10 accuracy for cross-scanner and cross-staining pairs and use $n = 8139$ tiles which is the reference value reported in the repository. The official Plismbench leaderboard [63] reports results for either the CLS+MEAN or the CLS token per model. Here, we report results for both the CLS+MEAN (in Table 1) and CLS tokens (in Table 4). Further details can be found in Appendix A.1.

Patho-Bench The Patho-Bench framework [81] is composed of 95 benchmark tasks covering seven subcategories: morphological subtyping, TME characterization, tumor grading, molecular subtyping, mutation prediction, treatment response assessment, and survival prediction. We evaluate a subset of 53 tasks drawn from multiple datasets using the ABMIL evaluation protocol using the default implementation [61]. The task selection is determined by implementation difficulties and dataset access. Performance is evaluated using task-appropriate metrics defined in the Patho-Bench protocol: area under the receiver operating characteristic curve (AUROC) for binary classification tasks, balanced accuracy for multi-class classification tasks, concordance index (C-index) for survival prediction tasks, and quadratic weighted Cohen’s kappa for tumor grading tasks. While Patho-Bench fixes the data splits, variance can be a result of the initialization and optimization of the ABMIL prediction head. To mitigate this, each task is performed three times and we report the mean of performance metrics across all data folds and random seeds. Evaluation results are presented using the provided data splits and task metadata on HuggingFace¹. Further details are reported in Appendix A.1.

Additional benchmarks The public benchmarks MSI CRC [42, 36], MSI STAD [42, 36], and TCGA Uniform [47] are not part of any public evaluation framework. For these benchmarks, we report an evaluation based on an internal framework. For each benchmark, we apply linear probing using logistic regression. Results are computed for 5 seeds over data split, shuffling, and initialization of the prediction head per foundation model and task. The mean across seeds is reported. Dataset splits are described in detail in Appendix A.1.

4 Results

The following analysis is based on eighty public benchmark datasets from five public foundation model evaluation frameworks *eva* [27], HEST [34], Plismbench [22], PathoROB [48], and Patho-Bench [81] as well as additional tumor-micro-environment (TME) and MSI prediction benchmark datasets. The tasks range from TME tissue- and cell-typing over identifying morphological patterns, identifying cancer subtypes, to predicting gene mutations from histology. The evaluation protocols and task descriptions are detailed in Section 3.3 and Appendix A.1, respectively.

4.1 Comparison of large-scale pathology foundation models

Table 1 shows that Atlas 2 achieves the best performance in 22/27 tasks and second best performance in 3 additional tasks with an average performance score of 44.8% on HEST, a 1.6 p.p. improvement compared to the second best performing model Pluto-4G [60], 82.9% on *eva*², a 1.2 p.p. improvement over the closest contender Pluto-4G [60], and an average robustness score of 85.7%, a 9.7 p.p. improvement to the closest contender Virchow2 [82]. Only a limited comparison to the recent model H-Optimus-1 [8] is possible. The results in Table 4 demonstrate that Atlas 2 performs better than H-Optimus-1 [8] on the shared benchmarks HEST, CRC-100k, and MHIST with an improvement of 1, 1.5, and 4.5. p.p., respectively.

¹<https://huggingface.co/datasets/MahmoodLab/Patho-Bench>

²For comparability this considers the benchmark subset of *eva* evaluated in [60].

	Atlas 2	Pluto-4G*	Atlas	UNI2-H	H.Optimus-0	Midnight-12k	Virchow2	Prov.GigaPath	UNI	Phikon-v2
HEST-ccRCC	27.9	-	29.5	28.1	<u>29.2</u>	20.9	27.2	24.9	25.1	27.4
HEST-COAD	34.9	-	29.3	<u>33.2</u>	30.9	31.8	25.8	32.0	25.8	25.6
HEST-IDC	62.7	-	60.4	<u>60.5</u>	<u>61.1</u>	59.9	<u>59.7</u>	58.1	58.5	56.8
HEST-LUNG	59.4	-	58.1	57.4	<u>57.5</u>	<u>58.3</u>	56.8	56.1	55.6	55.0
HEST-LYMPH-IDC	28.6	-	26.2	27.4	26.6	<u>27.5</u>	25.7	25.0	25.8	24.8
HEST-PAAD	54.2	-	51.7	<u>52.3</u>	51.1	<u>50.2</u>	47.8	49.9	48.8	47.7
HEST-PRAD	39.7	-	38.6	<u>37.5</u>	36.2	37.1	35.3	<u>39.1</u>	32.7	37.9
HEST-RECTUM	25.4	-	22.6	22.7	<u>24.0</u>	20.3	20.7	19.4	17.6	18.7
HEST-SKCM	70.0	-	62.0	<u>68.3</u>	<u>66.1</u>	64.8	64.0	59.7	62.3	58.4
MSI CRC (patch)	78.0	-	<u>72.6</u>	72.0	70.0	70.8	71.9	69.5	69.7	68.3
MSI STAD (patch)	76.1	-	73.0	73.1	72.2	<u>73.7</u>	72.5	68.1	68.6	69.2
HEST-Average	44.8	<u>43.2</u>	42.0	43.0	42.5	41.2	40.3	40.5	39.1	39.1
Molecular-Average	50.6	-	47.6	<u>48.4</u>	47.7	46.8	46.1	45.6	44.6	44.5
<hr/>										
BACH	91.7	93.2	<u>92.3</u>	92.2	74.7	90.6	88.6	79.2	79.7	73.6
BreakHis	88.3	81.8	89.9	86.3	81.0	83.4	81.1	84.5	80.4	70.9
CoNSeP	66.1	65.0	<u>65.1</u>	63.6	64.5	62.4	64.5	63.0	63.0	62.9
CRC-100k	97.2	96.8	<u>96.9</u>	<u>96.9</u>	96.4	<u>96.7</u>	96.6	<u>95.9</u>	96.1	95.3
Gleason	80.7	78.5	78.4	<u>77.6</u>	77.3	<u>79.0</u>	78.5	72.7	76.0	75.3
MHIST	88.5	<u>87.9</u>	86.8	82.6	85.1	81.2	86.5	83.3	83.8	79.6
MoNuSAC	69.4	70.4	67.4	64.5	68.1	65.8	66.8	66.4	65.0	64.3
PANDA	68.3	<u>66.6</u>	66.4	66.2	66.2	65.4	64.7	65.0	65.4	62.1
PCAM	96.1	<u>95.2</u>	<u>95.2</u>	95.1	94.4	93.0	93.9	94.6	93.9	90.0
CAMELYON16 (0.25 MPP)	86.8	-	<u>86.3</u>	85.9	84.7	86.1	85.7	80.7	84.1	80.7
TCGA Uniform (1.0 MPP)	84.1	-	78.7	79.4	76.0	<u>83.7</u>	78.0	74.7	74.3	70.1
TCGA Uniform (0.5 MPP)	82.7	-	77.0	78.8	78.8	83.2	77.5	74.3	74.5	76.7
Morphology-Average-Pluto-4G	82.9	81.7	<u>82.0</u>	80.6	78.6	79.7	80.1	78.3	78.1	74.9
Morphology-Average	83.3	-	<u>81.7</u>	80.8	78.9	80.9	80.2	77.9	78.0	75.1
<hr/>										
Prediction-Average-Pluto-4G	63.8	<u>62.5</u>	62.0	61.8	60.6	60.5	60.2	59.4	58.6	57.0
Prediction-Average	67.7	-	<u>65.4</u>	65.3	64.0	64.6	63.9	62.4	62.0	60.5
<hr/>										
Robustness Index (Camelyon)	94.0	-	78.5	54.4	70.5	47.8	<u>79.9</u>	38.2	14.5	1.9
Robustness Index (TCGA)	87.9	-	82.6	80.3	81.2	<u>85.8</u>	<u>82.2</u>	73.7	74.7	61.9
Robustness Index (Tolkach)	96.4	-	93.8	92.3	91.8	94.1	<u>95.4</u>	74.6	90.2	76.8
Plismbench (Leaderboard metric)	64.5	-	41.1	36.0	<u>52.2</u>	37.3	46.4	37.3	38.5	19.6
Robustness-Average	85.7	-	74.0	65.8	73.9	66.2	<u>76.0</u>	56.0	54.5	40.0

*Results for Pluto-4G taken from [60].

Table 1: The three sections of the table show prediction results for task with morphology and molecular targets as well as for robustness benchmarks. The **best** result per row is in bold, the second best result is underlined. The presented model Atlas 2 exhibits best performance on the majority of the tasks across all three sections.

In Table 2 we report additional analyses for molecular and morphology related tasks using the Patho-Bench framework [81]. Results demonstrate that Atlas 2 is the best performing model in 15/24 molecular related tasks and achieves at least second best performance in 19/24 molecular related tasks with an average improvement of 3.6 p.p. compared to the second best model, Virchow2. For morphology related benchmarks, Atlas 2 is the top performing model in 14/19 tasks and achieves at least second best performance in 16/19 tasks with an average difference of 3.3 p.p. compared to the second best model. Similarly, Atlas 2 shows the highest performance in treatment response prediction tasks with a 1.8 p.p. improvement compared to the second best performing model. For survival prediction tasks, H-Optimus-0 [67] is the best performing model, but it is noteworthy that all models perform close to the chance level (C-Index of 50) for this task.

	Atlas 2	Virchow2	Atlas	UNI2-H	H-Optimus-0
[CPTAC BRCA: Breast][Macro OvR AUC] Mutation prediction: TP53	83.6	<u>78.7</u>	78.2	77.7	76.0
[CPTAC BRCA: Breast][Macro OvR AUC] Mutation prediction: PIK3CA	59.6	58.2	59.4	61.1	<u>59.9</u>
[CPTAC CCRCC: Kidney][Macro OvR AUC] Mutation prediction: BAP1	70.4	67.4	70.5	66.9	65.3
[CPTAC CCRCC: Kidney][Macro OvR AUC] Mutation prediction: PBRM1	52.4	<u>49.4</u>	48.8	41.6	44.0
[CPTAC CCRCC: Kidney][Macro OvR AUC] Mutation prediction: VHL	52.9	<u>52.8</u>	48.7	48.2	49.7
[CPTAC COAD: Colon][Macro OvR AUC] Mutation prediction: KRAS	65.3	64.3	61.7	66.4	60.4
[CPTAC COAD: Colon][Macro OvR AUC] Mutation prediction: ACVR2A	84.5	78.2	76.9	75.7	<u>79.5</u>
[CPTAC COAD: Colon][Macro OvR AUC] Mutation prediction: APC	77.8	72.9	<u>74.7</u>	73.8	71.5
[CPTAC COAD: Colon][Macro OvR AUC] Mutation prediction: ARID1A	75.8	71.1	74.0	69.7	<u>75.6</u>
[CPTAC COAD: Colon][Macro OvR AUC] Mutation prediction: MSL_H	93.9	85.9	84.6	<u>89.0</u>	87.1
[CPTAC COAD: Colon][Macro OvR AUC] Mutation prediction: PIK3CA	62.2	<u>63.7</u>	57.1	59.1	63.9
[CPTAC COAD: Colon][Macro OvR AUC] Mutation prediction: SETD1B	82.3	75.3	76.0	79.9	<u>81.8</u>
[CPTAC COAD: Colon][Macro OvR AUC] Mutation prediction: TP53	72.5	66.1	62.3	<u>67.3</u>	67.1
[CPTAC GBM: Brain][Macro OvR AUC] Mutation prediction: EGFR	69.2	<u>62.1</u>	59.1	<u>57.5</u>	58.0
[CPTAC GBM: Brain][Macro OvR AUC] Mutation prediction: TP53	85.5	74.8	<u>83.7</u>	81.9	81.8
[CPTAC HNSC: Head&Neck][Macro OvR AUC] Mutation prediction: CASP8	65.8	56.6	<u>57.6</u>	60.1	54.9
[CPTAC LSCC: Lung][Macro OvR AUC] Mutation prediction: KEAP1	57.4	63.1	<u>63.4</u>	65.0	62.6
[CPTAC LSCC: Lung][Macro OvR AUC] Mutation prediction: ARID1A	46.9	41.9	42.6	<u>43.4</u>	41.8
[CPTAC LUAD: Lung][Macro OvR AUC] Mutation prediction: EGFR	81.0	81.7	<u>81.1</u>	77.1	77.8
[CPTAC LUAD: Lung][Macro OvR AUC] Mutation prediction: KRAS	70.4	73.9	66.9	65.4	<u>72.1</u>
[CPTAC LUAD: Lung][Macro OvR AUC] Mutation prediction: STK11	<u>88.5</u>	82.4	85.6	88.8	88.4
[CPTAC LUAD: Lung][Macro OvR AUC] Mutation prediction: TP53	<u>76.7</u>	77.3	69.6	76.0	71.4
[CPTAC PDA: Pancreas][Macro OvR AUC] Mutation prediction: SMAD4	47.6	44.6	<u>45.1</u>	37.0	41.4
[BC Therapy: Breast][Macro OvR AUC] Molecular Subtyping: HER2 status	69.9	<u>64.3</u>	60.9	63.6	61.2
Molecular-Average	70.5	<u>66.9</u>	66.2	66.3	66.4
<hr/>					
[CPTAC BRCA: Breast][Balanced Accuracy] TME Characterization: Immune class	59.3	<u>55.8</u>	51.7	53.8	52.2
[CPTAC CCRCC: Kidney][Balanced Accuracy] TME Characterization: Immune class	38.3	33.1	<u>35.7</u>	32.1	34.7
[CPTAC COAD: Colon][Balanced Accuracy] TME Characterization: Immune class	45.8	<u>42.1</u>	39.1	38.4	36.0
[CPTAC GBM: Brain][Balanced Accuracy] TME Characterization: Immune class	57.7	46.9	<u>52.0</u>	51.2	50.9
[CPTAC HNSC: Head&Neck][Balanced Accuracy] TME Characterization: Immune class	54.6	<u>51.5</u>	48.6	46.9	48.6
[CPTAC PDA: Pancreas][Balanced Accuracy] TME Characterization: Immune class	41.7	43.0	40.8	39.2	39.2
[CPTAC LSCC: Lung][Balanced Accuracy] TME Characterization: Immune class	57.8	<u>57.2</u>	54.2	50.7	53.7
[CPTAC LUAD: Lung][Balanced Accuracy] TME Characterization: Immune class	56.6	50.2	<u>50.3</u>	47.3	46.8
[Hancock: Head&Neck][Macro OvR AUC] TME Characterization: Lymphovascular invasion detection	69.9	64.8	<u>69.3</u>	65.4	68.0
[Hancock: Head&Neck][Macro OvR AUC] TME Characterization: Perineural invasion detection	74.0	72.3	71.8	68.5	<u>72.5</u>
[Hancock: Head&Neck][Macro OvR AUC] TME Characterization: Primary vs. Metastasis	65.8	65.0	61.9	<u>65.2</u>	62.6
[Hancock: Head&Neck][Balanced Accuracy] TME Characterization: Primary tumor site	77.5	<u>74.6</u>	74.1	73.9	74.4
[Hancock: Head&Neck][Macro OvR AUC] TME Characterization: Vascular invasion detection	67.6	63.0	66.9	<u>68.2</u>	70.4
[BC Therapy: Breast][Weighted Kappa] Tumor Grading	39.5	32.4	29.8	<u>34.9</u>	27.8
[CPTAC HNSC: Head&Neck][Weighted Kappa] Tumor Grading	36.1	36.0	29.8	36.6	33.6
[CPTAC LSCC: Lung][Weighted Kappa] Tumor Grading	22.7	22.1	23.8	26.7	<u>25.1</u>
[Hancock: Head&Neck][Weighted Kappa] Tumor Grading: Conventional Keratinizing	33.2	28.0	24.7	29.1	<u>30.9</u>
[Hancock: Head&Neck][Weighted Kappa] Tumor Grading: Conventional NonKeratinizing	23.7	20.4	20.6	<u>21.0</u>	18.1
[IMP Cervical: Cervix][Macro OvR AUC] Morphological subtyping	94.7	95.1	95.0	<u>95.4</u>	95.5
Morphology-Average	53.5	<u>50.2</u>	49.5	49.7	49.5
<hr/>					
[Boehmk: Ovary][C-Index] Survival prediction	51.7	50.8	49.5	<u>50.9</u>	49.2
[CPTAC CCRCC: Kidney][C-Index] Survival prediction	55.6	58.2	65.4	<u>63.8</u>	55.2
[CPTAC HNSC: Head&Neck][C-Index] Survival prediction	51.1	50.8	48.3	<u>56.7</u>	60.2
[CPTAC PDA: Pancreas][C-Index] Survival prediction	52.0	50.7	50.7	49.9	<u>51.3</u>
[CPTAC LUAD: Lung][C-Index] Survival prediction	52.2	57.1	52.5	48.1	<u>54.2</u>
[MBC: Breast][C-Index] Survival prediction	49.0	51.8	54.2	51.0	<u>53.0</u>
[Hancock: Head&Neck][C-Index] Survival prediction	57.0	56.4	56.5	53.9	<u>56.7</u>
Survival-Average	52.7	53.7	<u>53.9</u>	53.5	54.3
<hr/>					
[BC Therapy: Breast][Macro OvR AUC] Treatment response: ER status	76.4	66.1	69.2	<u>70.0</u>	60.5
[BC Therapy: Breast][Balanced Accuracy] Treatment Response: Residual cancer burden	33.7	29.0	29.5	<u>31.2</u>	27.4
[MBC: Breast][Weighted Kappa] Treatment Response: Recist	10.3	8.5	16.1	10.2	<u>12.1</u>
Treatment-Response-Average	40.1	34.5	<u>38.3</u>	37.1	33.3
<hr/>					
Prediction-Average	60.3	<u>57.4</u>	57.0	57.0	56.9

Table 2: The four sections of the table show prediction results for task with morphology, molecular, survival, and treatment targets from the Patho-Bench [81] framework. The **best** result per row is in bold, the second best result is underlined. The presented model Atlas 2 exhibits best performance on the majority of the tasks across three sections. For survival prediction H-Optimus-0 [67] shows best performance, but it is to note that all models perform close to chance level (C-Index 50).

	Atlas 2	ViT-B					ViT-S				
		Atlas 2-B	ViT-B/8 [1]	Hibou-B	Phnkon	H0-mini*	Atlas 2-S	Pluto-4S-8*	Pluto-4S-16*	ViT-S/8 [37]	ViT-S/8 [1]
HEST-ccRCC	27.9	<u>26.0</u>	24.8	22.8	24.2	26.4	24.8	-	-	26.7	<u>25.7</u>
HEST-COAD	34.9	32.4	<u>30.2</u>	28.7	27.8	27.0	<u>27.9</u>	-	-	30.2	23.0
HEST-IDC	62.7	60.8	57.0	56.0	54.8	<u>59.1</u>	58.9	-	-	<u>55.2</u>	54.5
HEST-LUNG	59.4	<u>56.6</u>	53.9	54.9	56.7	56.3	56.4	-	-	<u>54.4</u>	53.2
HEST-LYMPH-IDC	28.6	26.6	23.5	25.0	23.8	<u>26.4</u>	25.2	-	-	<u>24.9</u>	23.9
HEST-PAAD	54.2	52.3	47.8	45.9	46.5	<u>50.7</u>	46.6	-	-	<u>44.2</u>	43.3
HEST-PRAD	39.7	38.1	<u>38.0</u>	30.6	34.5	36.3	<u>36.9</u>	-	-	27.1	<u>34.4</u>
HEST-RECTUM	25.4	<u>22.2</u>	17.0	17.6	16.6	<u>20.5</u>	<u>16.8</u>	-	-	<u>15.5</u>	14.4
HEST-SKCM	70.0	65.1	59.4	55.9	54.5	<u>61.2</u>	60.8	-	-	<u>57.5</u>	56.5
MSI CRC (patch)	78.0	75.4	<u>68.8</u>	68.3	67.2	-	70.8	-	-	<u>70.2</u>	69.4
MSI STAD (patch)	76.1	74.3	68.1	<u>71.0</u>	67.1	-	76.0	-	-	<u>72.6</u>	72.3
HEST-Average	44.8	42.2	39.1	37.5	37.7	<u>40.4</u>	39.4	36.9	36.4	<u>37.3</u>	36.5
Molecular-Average	50.6	48.2	<u>44.4</u>	43.3	43.1	-	45.6	-	-	<u>43.5</u>	42.8
<hr/>											
BACH	91.7	90.0	88.0	81.9	73.5	-	90.1	<u>85.1</u>	79.8	77.3	80.2
BreakHis	88.3	<u>81.3</u>	84.4	79.8	71.0	-	86.6	<u>80.8</u>	76.8	72.7	73.0
CoNSeP	66.1	66.2	<u>64.5</u>	63.3	62.8	62.9	65.2	<u>64.9</u>	62.1	63.4	63.9
CRC-100k	97.2	97.0	96.0	95.8	94.7	-	96.8	95.4	<u>95.5</u>	94.9	95.1
Gleason	80.7	79.4	<u>75.4</u>	73.6	74.2	-	77.1	76.3	<u>76.6</u>	74.3	73.3
MHIST	88.5	86.9	<u>83.0</u>	79.9	82.3	-	84.9	<u>84.2</u>	83.4	76.5	82.7
MoNuSAC	69.4	69.2	<u>68.5</u>	64.9	64.3	64.3	68.9	<u>67.8</u>	64.0	66.7	65.3
PANDA	68.3	68.7	<u>64.7</u>	63.2	64.5	-	66.3	<u>63.1</u>	63.0	61.9	60.3
PCAM	96.1	94.7	92.0	<u>94.3</u>	92.8	-	93.9	91.4	91.6	<u>92.4</u>	88.6
CAMELYON16 (0.25 MPP)	86.8	85.4	81.9	80.3	<u>82.8</u>	-	84.7	-	-	<u>79.1</u>	<u>81.1</u>
TCGA Uniform (1.0 MPP)	84.1	<u>80.0</u>	80.5	72.4	<u>70.8</u>	-	74.7	-	-	71.9	<u>74.0</u>
TCGA Uniform (0.5 MPP)	82.7	<u>78.1</u>	79.2	71.1	75.6	-	72.3	-	-	71.5	<u>72.2</u>
Morphology-Average-Pluto-4G	82.9	81.5	<u>79.6</u>	77.4	75.6	-	81.1	<u>78.8</u>	77.0	75.6	75.8
Morphology-Average	83.3	81.4	<u>79.8</u>	76.7	75.8	-	80.1	-	-	75.2	<u>75.8</u>
<hr/>											
Prediction-Average-Pluto-4G	63.8	61.9	<u>59.3</u>	57.4	56.6	-	60.2	<u>57.8</u>	56.7	56.4	56.2
Prediction-Average	67.7	65.5	<u>62.9</u>	60.7	60.1	-	63.6	-	-	<u>60.0</u>	<u>60.0</u>
<hr/>											
Robustness Index (Camelyon)	94.0	87.3	14.7	5.2	1.1	<u>71.8</u>	84.5	-	-	4.3	<u>26.5</u>
Robustness Index (TCGA)	87.9	83.2	76.3	61.3	62.3	<u>79.4</u>	80.3	-	-	66.1	<u>74.0</u>
Robustness Index (Tolkach)	96.4	95.5	89.6	79.5	79.5	<u>93.2</u>	95.8	-	-	83.2	<u>91.8</u>
Plismbench (Leaderboard metric)	64.5	67.4	<u>35.8</u>	24.6	24.4	-	67.7	-	-	32.1	<u>37.4</u>
Robustness-Average	85.7	83.4	<u>54.1</u>	42.6	41.8	-	82.1	-	-	46.4	<u>57.4</u>

*Results for H0-mini taken from [22] (HEST, eva) and [62] (PathoROB). Results for Pluto-4S-8 and Pluto-4S-16 taken from [60].

Table 3: Comparison of resource efficient pathology foundation models for the same benchmarks as in Table 1. To better compare models of similar sizes, we highlight the **best** and second-best results per task for each architecture (ViT-B and ViT-S) separately. Atlas 2-B and 2-S exhibit best performance in their respective architecture category on the majority of tasks.

4.2 Comparison of resource efficient pathology foundation models

Table 3 shows results for resource efficient models. Atlas 2-B and Atlas 2-S are distilled from Atlas 2 and are 24 and 91 times smaller in parameter size and 3.4 and 9 times more resource efficient for a standard-size image inference. The results show that Atlas 2-B and Atlas 2-S are the best performing models in 22/27 and 25/27 tasks and at least second best in 27/27 and 26/27 respectively in their respective compute category. Despite being more resource efficient, Atlas 2-B performs similar to or on par with larger models Atlas [2], and UNI2-H [13] and outperforms the larger models H-Optimus-0 [67], Midnight-12k [39], and Virchow2 [82]. Atlas 2-S achieves similar performance as H-Optimus-0 [67], Midnight-12k [39], and Virchow2 [82] despite being 4.3-7.4 times more resource efficient for a standard-size image inference. The models also show significantly better robustness with an improvement of 29.3 p.p. and 24.7 p.p. compared to the second best model, respectively.

Due to a lack of reference values and model access, H0-mini [23] could not be compared on each robustness benchmark. A comparison to H0-mini [23] on published results shows that for the CLS+MEAN representation the average robustness on PathoROB [48] is 7.2 p.p. better for Atlas 2-B (88.7 vs. 81.5). On the CLS token evaluation for Plismbench [22], Atlas 2-B outperforms H0-mini by nearly 10 p.p. (63.9 vs. 54.1).

5 Discussion

For clinical deployment, foundation models must demonstrate both high prediction performance for the task at hand and robustness to confounding data variations commonly seen in routine diagnostics. Additionally, the large volume of histological slides produced in pathology labs necessitates efficient processing to provide timely and cost-effective analyses. Our novel pathology foundation models Atlas 2, as well as its efficient, distilled versions 2-B and 2-S were trained on the to date largest dataset used for pathology foundation model development comprising 5.5 million histological slides. Our models show consistent state of the art performance on all three important requirements — prediction performance, robustness, and resource efficiency. The evaluation was performed on eighty benchmarks from five different public benchmark suits covering a wide variety of tasks, datasets, and tissue types. While further improvements and benchmarking are warranted, our models outperform all other evaluated pathology foundation models on the vast majority of benchmarks and demonstrate that tradeoffs for clinical deployments of pathology foundation models can effectively be minimized.

Acknowledgments

We would like to thank the teams at Aignostics, Charité - Universitätsmedizin Berlin - Pathology Department, LMU Munich - Pathology Department, Mayo Clinic Digital Pathology, Mayo Clinic Generative Artificial Intelligence Program, Mayo HPC team, and Mayo Clinic Department of Laboratory Medicine and Pathology for supporting this work. Special thanks goes to Edwin de Jong, Pavel Trunov, Paul Mattes, Evelyn Ramberger, Hans Pinckaers, Sergey Melnik, Steele Clifton-Berry, Viktor Matyas, Crystal D. Liudahl, Zach D. Jensen, and Wyman D. Matthews for their organizational, technical, and other support.

The benchmark results shown here are in part based upon data generated by the TCGA Research Network: <https://www.cancer.gov/tcga>.

This work was in part supported by the German Ministry for Education and Research (BMBF) under Grants 01IS14013A-E, 01GQ1115, 01GQ0850, 01IS18025A, 031L0207D, and 01IS18037A. K.R.M. was partly supported by the Institute of Information & Communications Technology Planning & Evaluation (IITP) grants funded by the Korea government (MSIT) (No. 2019-0-00079, Artificial Intelligence Graduate School Program, Korea University and No. 2022-0-00984, Development of Artificial Intelligence Technology for Personalized Plug-and-Play Explanation and Verification of Explanation).

References

- [1] Nanne Aben, Edwin D. de Jong, Ioannis Gatopoulos, Nicolas Käenzig, Mikhail Karasikov, Axel Lagré, Roman Moser, Joost van Doorn, and Fei Tang. Towards Large-Scale Training of Pathology Foundation Models, March 2024. arXiv:2404.15217.
- [2] Maximilian Alber, Stephan Tietz, Jonas Dippel, Timo Milbich, Timothée Lesort, Panos Korfiatis, Moritz Krügener, Beatriz Perez Cancer, Neelay Shah, Alexander Möllers, Philipp Seegerer, Alexandra Carpen-Amarie, Kai Standvoss, Gabriel Dernbach, Edwin de Jong, Simon Schallenberg, Andreas Kunft, Helmut Hoffer von Ankershoffen, Gavin Schaeferle, Patrick Duffy, Matt Redlon, Philipp Jurmeister, David Horst, Lukas Ruff, Klaus-Robert Müller, Frederick Klauschen, and Andrew Norgan. Atlas: A novel pathology foundation model by mayo clinic, charité, and aignostics, 2025.
- [3] Guilherme Aresta, Teresa Araújo, Scotty Kwok, Sai Saketh Chennamsetty, Mohammed Safwan, Varghese Alex, Bahram Marami, Marcel Prastawa, Monica Chan, Michael Donovan, et al. BACH: Grand challenge on breast cancer histology images. *Medical image analysis*, 56:122–139, 2019.

- [4] Eirini Arvaniti, Kim Fricker, Michael Moret, Niels Rupp, Thomas Hermanns, Christian Fankhauser, Norbert Wey, Peter Wild, Jan Rueschoff, and Manfred Claassen. Automated gleason grading of prostate cancer tissue microarrays via deep learning, 03 2018.
- [5] Babak Ehteshami Bejnordi, Mitko Veta, Paul Johannes Van Diest, Bram Van Ginneken, Nico Karssemeijer, Geert Litjens, Jeroen AWM Van Der Laak, Meyke Hermsen, Quirine F Manson, Maschenka Balkenhol, et al. Diagnostic assessment of deep learning algorithms for detection of lymph node metastases in women with breast cancer. *JAMA*, 318(22):2199–2210, 2017.
- [6] Lucas Beyer, Xiaohua Zhai, Amélie Royer, Larisa Markeeva, Rohan Anil, and Alexander Kolesnikov. Knowledge distillation: A good teacher is patient and consistent. In *Proceedings of the IEEE/CVF Conference on Computer Vision and Pattern Recognition (CVPR)*, 2022.
- [7] Alexander Binder, Michael Bockmayr, Miriam Hägele, Stephan Wienert, Daniel Heim, Katharina Hellweg, Masaru Ishii, Albrecht Stenzinger, Andreas Hocke, Carsten Denkert, et al. Morphological and molecular breast cancer profiling through explainable machine learning. *Nature Machine Intelligence*, 3(4):355–366, 2021.
- [8] Bioptimus. H-optimus-1. <https://huggingface.co/bioptimus/H-optimus-1>, 2025.
- [9] Wouter Bulten, Kimmo Kartasalo, Po-Hsuan Cameron Chen, Peter Ström, Hans Pinckaers, Kunal Nagpal, Yuannan Cai, David F Steiner, Hester Van Boven, Robert Vink, et al. Artificial intelligence for diagnosis and gleason grading of prostate cancer: the PANDA challenge. *Nature medicine*, 28(1):154–163, 2022.
- [10] Péter Bándi, Oscar Geessink, Quirine Manson, Marcory Van Dijk, Maschenka Balkenhol, Meyke Hermsen, Babak Ehteshami Bejnordi, Byungjae Lee, Kyunghyun Paeng, Aoxiao Zhong, Quanzheng Li, Farhad Ghazvinian Zanjani, Svitlana Zinger, Keisuke Fukuta, Daisuke Komura, Vlado Ovtcharov, Shenghua Cheng, Shaoqun Zeng, Jeppe Thagaard, Anders B. Dahl, Huangjing Lin, Hao Chen, Ludwig Jacobsson, Martin Hedlund, Melih Çetin, Eren Halıcı, Hunter Jackson, Richard Chen, Fabian Both, Jörg Franke, Heidi Küsters-Vandevelde, Willem Vreuls, Peter Bult, Bram van Ginneken, Jeroen van der Laak, and Geert Litjens. From detection of individual metastases to classification of lymph node status at the patient level: The camelyon17 challenge. *IEEE Transactions on Medical Imaging*, 38(2):550–560, 2019.
- [11] Gianluca Carloni, Biagio Brattoli, Seongho Keum, Jongchan Park, Taebum Lee, Chang Ho Ahn, and Sergio Pereira. Pathology foundation models are scanner sensitive: Benchmark and mitigation with contrastive scangen loss. In *International Workshop on Foundation Models for General Medical AI*, pages 44–53. Springer, 2025.
- [12] Binghao Chai, Jianan Chen, Paul Cool, Fatine Oumlil, Anna Tollitt, David F Steiner, Tapabrata Chakraborti, and Adrienne M Flanagan. Impact of tissue staining and scanner variation on the performance of pathology foundation models: a study of sarcomas and their mimics. *bioRxiv*, pages 2025–08, 2025.
- [13] Richard J. Chen, Tong Ding, Ming Y. Lu, Drew F. K. Williamson, Guillaume Jaume, Andrew H. Song, Bowen Chen, Andrew Zhang, Daniel Shao, Muhammad Shaban, Mane Williams, Lukas Oldenburg, Luca L. Weishaupt, Judy J. Wang, Anurag Vaidya, Long Phi Le, Georg Gerber, Sharifa Sahai, Walt Williams, and Faisal Mahmood. Towards a general-purpose foundation model for computational pathology. *Nature Medicine*, 30(3):850–862, March 2024.
- [14] Edwin D de Jong, Eric Marcus, and Jonas Teuwen. Current pathology foundation models are unrobust to medical center differences. *arXiv preprint arXiv:2501.18055*, 2025.
- [15] James A Diao, Jason K Wang, Wan Fung Chui, Victoria Mountain, Sai Chowdary Gullapally, Ramprakash Srinivasan, Richard N Mitchell, Benjamin Glass, Sara Hoffman, Sudha K Rao, et al. Human-interpretable image features derived from densely mapped cancer pathology slides predict diverse molecular phenotypes. *Nature communications*, 12(1):1613, 2021.
- [16] Tong Ding, Sophia J Wagner, Andrew H Song, Richard J Chen, Ming Y Lu, Andrew Zhang, Anurag J Vaidya, Guillaume Jaume, Muhammad Shaban, Ahrong Kim, et al. A multimodal whole-slide foundation model for pathology. *Nature Medicine*, pages 1–13, 2025.

[17] Jonas Dippel, Barbara Feulner, Tobias Winterhoff, Timo Milbich, Stephan Tietz, Simon Schallenberg, Gabriel Dernbach, Andreas Kunft, Simon Heinke, Marie-Lisa Eich, Julika Ribbat-Idel, Rosemarie Krupar, Philipp Anders, Niklas Preni  l, Philipp Jurmeister, David Horst, Lukas Ruff, Klaus-Robert M  ller, Frederick Klauschen, and Maximilian Alber. RudolfV: A Foundation Model by Pathologists for Pathologists, June 2024. arXiv:2401.04079.

[18] Jonas Dippel, Niklas Preni  l, Julius Hense, Philipp Liznerski, Tobias Winterhoff, Simon Schallenberg, Marius Kloft, Oliver Buchstab, David Horst, Maximilian Alber, Lukas Ruff, Klaus-Robert M  ller, and Frederick Klauschen. Ai-based anomaly detection for clinical-grade histopathological diagnostics. *NEJM AI*, 1(11):A1oa2400468, 2024.

[19] Alexey Dosovitskiy, Lucas Beyer, Alexander Kolesnikov, Dirk Weissenborn, Xiaohua Zhai, Thomas Unterthiner, Mostafa Dehghani, Matthias Minderer, Georg Heigold, Sylvain Gelly, Jakob Uszkoreit, and Neil Houlsby. An image is worth 16x16 words: Transformers for image recognition at scale. *ICLR*, 2021.

[20] David Jacob Drexlin, Jonas Dippel, Julius Hense, Niklas Preni  l, Gr  goire Montavon, Frederick Klauschen, and Klaus-Robert M  ller. Medi: Metadata-guided diffusion models for mitigating biases in tumor classification. *International Conference on Medical Image Computing and Computer-Assisted Intervention*, pages 379–388, 2025.

[21] eva: Evaluation framework for oncology foundation models (FMs). <https://github.com/kaiko-ai/eva/tree/0.4.2>, 2025. v0.4.2.

[22] Alexandre Filiot, Nicolas Dop, Oussama Tchita, Auriane Riou, R  my Dubois, Thomas Peeters, Daria Valter, Marin Scalbert, Charlie Saillard, Genevi  e Robin, and Antoine Olivier. Distilling foundation models for robust and efficient models in digital pathology. In James C. Gee, Daniel C. Alexander, Jaesung Hong, Juan Eugenio Iglesias, Carole H. Sudre, Archana Venkataraman, Polina Golland, Jong Hyo Kim, and Jinah Park, editors, *Medical Image Computing and Computer Assisted Intervention – MICCAI 2025*, pages 162–172, Cham, 2026. Springer Nature Switzerland.

[23] Alexandre Filiot, Nicolas Dop, Oussama Tchita, Auriane Riou, Thomas Peeters, Daria Valter, Marin Scalbert, Charlie Saillard, Genevi  e Robin, and Antoine Olivier. Distilling foundation models for robust and efficient models in digital pathology, 2025.

[24] Alexandre Filiot, Ridouane Ghermi, Antoine Olivier, Paul Jacob, Lucas Fidon, Alice Mac Kain, Charlie Saillard, and Jean-Baptiste Schiratti. Scaling self-supervised learning for histopathology with masked image modeling. *medRxiv*, 2023.

[25] Alexandre Filiot, Paul Jacob, Alice Mac Kain, and Charlie Saillard. Phikon-v2, A large and public feature extractor for biomarker prediction, September 2024. arXiv:2409.09173.

[26] Yaroslav Ganin, Evgeniya Ustinova, Hana Ajakan, Pascal Germain, Hugo Larochelle, Fran  ois Laviolette, Mario Marchand, and Victor S. Lempitsky. Domain-adversarial training of neural networks. *J. Mach. Learn. Res.*, 17:59:1–59:35, 2016.

[27] Ioannis Gatopoulos, Nicolas K  anzig, Roman Moser, and Sebastian Ot  lora. eva: Evaluation framework for pathology foundation models. In *Medical Imaging with Deep Learning*, 2024.

[28] Simon Graham, Quoc Dang Vu, Shan E Ahmed Raza, Jin Tae Kwak, and Nasir M. Rajpoot. XY network for nuclear segmentation in multi-tissue histology images. *CoRR*, abs/1812.06499, 2018.

[29] Fredrik K Gustafsson and Mattias Rantalainen. Evaluating computational pathology foundation models for prostate cancer grading under distribution shifts. *arXiv preprint arXiv:2410.06723*, 2024.

[30] Hest-library: Bringing spatial transcriptomics and histopathology together. <https://github.com/mahmoodlab/HEST/tree/v1.2.0>, 2024. v1.2.0.

[31] Geoffrey Hinton, Oriol Vinyals, and Jeff Dean. Distilling the knowledge in a neural network. In *NeurIPS 2014 - Deep Learning Workshop*, 2015.

- [32] Maximilian Ilse, Jakub Tomczak, and Max Welling. Attention-based deep multiple instance learning. In *International Conference on Machine Learning*, pages 2127–2136, 2018.
- [33] Maximilian Ilse, Jakub M. Tomczak, and Max Welling. Attention-based deep multiple instance learning, 2018.
- [34] Guillaume Jaume, Paul Doucet, Andrew H. Song, Ming Y. Lu, Cristina Almagro Pérez, Sophia J Wagner, Anurag Jayant Vaidya, Richard J. Chen, Drew FK Williamson, Ahrong Kim, and Faisal Mahmood. HEST-1k: A dataset for spatial transcriptomics and histology image analysis. In *The Thirty-eight Conference on Neural Information Processing Systems Datasets and Benchmarks Track*, 2024.
- [35] Dinkar Juyal, Harshith Padigela, Chintan Shah, Daniel Shenker, Natalia Harguindeguy, Yi Liu, Blake Martin, Yibo Zhang, Michael Nercessian, Miles Markey, Isaac Finberg, Kelsey Luu, Daniel Borders, Syed Ashar Javed, Emma L Krause, Raymond Biju, Aashish Sood, Allen Ma, Jackson Nyman, John Shamshoian, Guillaume Chhor, Darpan Sanghavi, Marc Thibault, Limin Yu, Fedaa Najdawi, Jennifer A. Hipp, Darren Fahy, Benjamin Glass, Eric Walk, John Abel, Harsha Vardhan pokkalla, Andrew H. Beck, and Sean Grullon. PLUTO: Pathology-universal transformer. In *ICML 2024 Workshop on Efficient and Accessible Foundation Models for Biological Discovery*, 2024.
- [36] Jakub R Kaczmarzyk, Rajarsi Gupta, Tahsin M Kurc, Shahira Abousamra, Joel H Saltz, and Peter K Koo. Champkit: A framework for rapid evaluation of deep neural networks for patch-based histopathology classification. *Computer methods and programs in biomedicine*, 239:107631, 2023.
- [37] Mingu Kang, Heon Song, Seonwook Park, Donggeun Yoo, and Sérgio Pereira. Benchmarking self-supervised learning on diverse pathology datasets. In *Proceedings of the IEEE/CVF Conference on Computer Vision and Pattern Recognition (CVPR)*, June 2023.
- [38] Daniel Kaplan, Ratna Sagari Grandhi, Connor Lane, Benjamin Warner, Tanishq Mathew Abraham, and Paul S. Scotti. How to train a state-of-the-art pathology foundation model with \$1.6k, 2025.
- [39] Mikhail Karasikov, Joost van Doorn, Nicolas Käenzig, Melis Erdal Cesur, Hugo Mark Horlings, Robert Berke, Fei Tang, and Sebastian Ottálora. Training state-of-the-art pathology foundation models with orders of magnitude less data. In *Medical Image Computing and Computer Assisted Intervention – MICCAI 2025*, volume LNCS 15967, pages 573–583. Springer Nature Switzerland, October 2025.
- [40] Jakob Nikolas Kather, Niels Halama, and Alexander Marx. 100,000 histological images of human colorectal cancer and healthy tissue (v0.1) [Data set]. Zenodo. <https://doi.org/10.5281/zenodo.1214456>, May 2018.
- [41] Jakob Nikolas Kather, Johannes Krisam, Pornpimol Charoentong, Tom Luedde, Esther Herpel, Cleo-Aron Weis, Timo Gaiser, Alexander Marx, Nektarios A Valous, Dyke Ferber, et al. Predicting survival from colorectal cancer histology slides using deep learning: A retrospective multicenter study. *PLoS medicine*, 16(1):e1002730, 2019.
- [42] Jakob Nikolas Kather, Alexander T Pearson, Niels Halama, Dirk Jäger, Jeremias Krause, Sven H Loosen, Alexander Marx, Peter Boor, Frank Tacke, Ulf Peter Neumann, et al. Deep learning can predict microsatellite instability directly from histology in gastrointestinal cancer. *Nature medicine*, 25(7):1054–1056, 2019.
- [43] Jacob Kauffmann, Jonas Dippel, Lukas Ruff, Wojciech Samek, Klaus-Robert Müller, and Grégoire Montavon. Explainable AI reveals Clever Hans effects in unsupervised learning models. *Nature Machine Intelligence*, 7:412—422, 2025.
- [44] Philipp Keyl, Michael Bockmayr, Daniel Heim, Gabriel Dernbach, Grégoire Montavon, Klaus-Robert Müller, and Frederick Klauschens. Patient-level proteomic network prediction by explainable artificial intelligence. *NPJ Precision Oncology*, 6(1):35, 2022.

[45] Frederick Klauschen, Jonas Dippel, Philipp Keyl, Philipp Jurmeister, Michael Bockmayr, Andreas Mock, Oliver Buchstab, Maximilian Alber, Lukas Ruff, Grégoire Montavon, et al. Toward explainable artificial intelligence for precision pathology. *Annual Review of Pathology: Mechanisms of Disease*, 19(1):541–570, 2024.

[46] Jonah Kömen, Hannah Marienwald, Jonas Dippel, and Julius Hense. Do histopathological foundation models eliminate batch effects? A comparative study. 2024. Presented at: NeurIPS 2024 Workshop on Advancements In Medical Foundation Models: Explainability, Robustness, Security, and Beyond.

[47] Daisuke Komura, Akihiro Kawabe, Keisuke Fukuta, Kyohei Sano, Toshikazu Umezaki, Hirotomo Koda, Ryohei Suzuki, Ken Tominaga, Mieko Ochi, Hiroki Konishi, et al. Universal encoding of pan-cancer histology by deep texture representations. *Cell Reports*, 38(9), 2022.

[48] Jonah Kömen, Edwin D. de Jong, Julius Hense, Hannah Marienwald, Jonas Dippel, Philip Naumann, Eric Marcus, Lukas Ruff, Maximilian Alber, Jonas Teuwen, Frederick Klauschen, and Klaus-Robert Müller. Towards robust foundation models for digital pathology, 2025.

[49] Sebastian Lapuschkin, Stephan Wäldchen, Alexander Binder, Grégoire Montavon, Wojciech Samek, and Klaus-Robert Müller. Unmasking Clever Hans predictors and assessing what machines really learn. *Nature Communications*, 10(1):1096, 2019.

[50] Tim Lenz, Peter Neidlinger, Marta Ligero, Georg Wölfllein, Marko van Treeck, and Jakob Nikolas Kather. Unsupervised foundation model-agnostic slide-level representation learning, 2024. arXiv:2411.13623.

[51] Weiping Lin, Shen Liu, Runchen Zhu, and Liansheng Wang. Unveiling institution-specific bias in pathology foundation models: Detriments, causes, and potential solutions. *arXiv preprint arXiv:2502.16889*, 2025.

[52] Ming Y Lu, Bowen Chen, Drew FK Williamson, Richard J Chen, Ivy Liang, Tong Ding, Guillaume Jaume, Igor Odintsov, Long Phi Le, Georg Gerber, et al. A visual-language foundation model for computational pathology. *Nature Medicine*, 30:863–874, 2024.

[53] Marc Macenko, Marc Niethammer, J. Marron, David Borland, John Woosley, Xiaojun Guan, Charles Schmitt, and Nancy Thomas. A method for normalizing histology slides for quantitative analysis. In *IEEE International Symposium on Biomedical Imaging: From Nano to Macro (ISBI)*, 2009.

[54] Alexander Möllers, Julius Hense, Florian Schulz, Timo Milbich, Maximilian Alber, and Lukas Ruff. Mind the gap: Continuous magnification sampling for pathology foundation models, 2026.

[55] Dmitry Nechaev, Alexey Pchelnikov, and Ekaterina Ivanova. Hibou: A Family of Foundational Vision Transformers for Pathology, June 2024. arXiv:2406.05074.

[56] Dmitry Nechaev, Alexey Pchelnikov, and Ekaterina Ivanova. Hibou: A family of foundational vision transformers for pathology, 2024.

[57] Hai Cao Truong Nguyen and David Joon Ho. fmMAP: A framework reducing site-bias batch effect from foundation models in pathology. In *MICCAI Workshop on Computational Pathology with Multimodal Data (COMPAYL)*, 2025.

[58] Masaki Ochi, Daisuke Komura, Takumi Onoyama, et al. Registered multi-device/staining histology image dataset for domain-agnostic machine learning models. *Scientific Data*, 11:330, 2024.

[59] Maxime Oquab, Timothée Darzet, Théo Moutakanni, Huy V. Vo, Marc Szafraniec, Vasil Khalidov, Pierre Fernandez, Daniel HAZIZA, Francisco Massa, Alaaeldin El-Nouby, Mido Assran, Nicolas Ballas, Wojciech Galuba, Russell Howes, Po-Yao Huang, Shang-Wen Li, Ishan Misra, Michael Rabbat, Vasu Sharma, Gabriel Synnaeve, Hu Xu, Herve Jegou, Julien Mairal, Patrick Labatut, Armand Joulin, and Piotr Bojanowski. DINOv2: Learning robust visual features without supervision. *Transactions on Machine Learning Research*, 2024. Featured Certification.

[60] Harshith Padigela, Shima Nofallah, Atchuth Naveen Chilaparasetti, Ryun Han, Andrew Walker, Judy Shen, Chintan Shah, Blake Martin, Aashish Sood, Elliot Miller, Ben Glass, Andy Beck, Harsha Pokkalla, and Syed Ashar Javed. Pluto-4: Frontier pathology foundation models, 2025.

[61] Patho-Bench: Standardized benchmark for computational pathology foundation models. <https://github.com/mahmoodlab/Patho-Bench/tree/660e77044640e3d7d2f1150cc6721e97454993bf>, 2025.

[62] Pathorob: Benchmark for pathology foundation models robustness to non-biological medical center differences. <https://github.com/bifold-pathomics/PathoROB/tree/ac1abe4df8c4d5b03aab13d6d9aabbc7205061e6>, 2025.

[63] Plismbench: A robustness benchmark of pathology foundation models. <https://github.com/owkin/plism-benchmark/tree/b4f32b7c233e0f5ba8340da89ef65803cf2ce49>, 2025.

[64] Zhongwei Qiu, Hanqing Chao, Tiancheng Lin, Wanxing Chang, Zijiang Yang, Wenpei Jiao, Yixuan Shen, Yunshuo Zhang, Yelin Yang, Wenbin Liu, Hui Jiang, Yun Bian, Ke Yan, Dakai Jin, and Le Lu. Bridging local inductive bias and long-range dependencies with pixel-mamba for end-to-end whole slide image analysis. In *Proceedings of the IEEE/CVF International Conference on Computer Vision (ICCV)*, pages 22738–22747, October 2025.

[65] Patricia Raciti, Jillian Sue, Juan A Retamero, Rodrigo Ceballos, Ran Godrich, Jeremy D Kunz, Adam Casson, Dilip Thiagarajan, Zahra Ebrahimzadeh, Julian Viret, et al. Clinical validation of artificial intelligence–augmented pathology diagnosis demonstrates significant gains in diagnostic accuracy in prostate cancer detection. *Archives of Pathology & Laboratory Medicine*, 147(10):1178–1185, 2023.

[66] Erik Reinhard, Michael Adhikhmin, Bruce Gooch, and Peter Shirley. Color transfer between images. *IEEE Computer Graphics and Applications*, 21(5):34–41, 2001.

[67] Charlie Saillard, Rodolphe Jenatton, Felipe Llinares-López, Zelda Mariet, David Cahané, Eric Durand, and Jean-Philippe Vert. H-optimus-0. <https://github.com/bioptimus/releases/tree/main/models/h-optimus/v0>, 2024.

[68] George Shaikovski, Adam Casson, Kristen Severson, Eric Zimmermann, Yi Kan Wang, Jeremy D. Kunz, Juan A. Retamero, Gerard Oakley, David Klimstra, Christopher Kanan, Matthew Hanna, Michal Zelechowski, Julian Viret, Neil Tenenholz, James Hall, Nicolo Fusi, Razik Yousfi, Peter Hamilton, William A. Moye, Eugene Vorontsov, Siqi Liu, and Thomas J. Fuchs. PRISM: A Multi-Modal Generative Foundation Model for Slide-Level Histopathology, May 2024. arXiv:2405.10254.

[69] Oriane Siméoni, Huy V. Vo, Maximilian Seitzer, Federico Baldassarre, Maxime Oquab, Cijo Jose, Vasil Khalidov, Marc Szafraniec, Seungeun Yi, Michaël Ramamonjisoa, Francisco Massa, Daniel Haziza, Luca Wehrstedt, Jianyuan Wang, Timothée Darcet, Théo Moutakanni, Leonel Sentana, Claire Roberts, Andrea Vedaldi, Jamie Tolan, John Brandt, Camille Couprie, Julien Mairal, Hervé Jégou, Patrick Labatut, and Piotr Bojanowski. DINOv3, 2025.

[70] Fabio A. Spanhol, Luiz S. Oliveira, Caroline Petitjean, and Laurent Heutte. A dataset for breast cancer histopathological image classification. *IEEE Transactions on Biomedical Engineering*, 63(7):1455–1462, 2016.

[71] Yuxuan Sun, Yixuan Si, Chenglu Zhu, Xuan Gong, Kai Zhang, Pingyi Chen, Ye Zhang, Zhongyi Shui, Tao Lin, and Lin Yang. Cpath-omni: A unified multimodal foundation model for patch and whole slide image analysis in computational pathology. In *Proceedings of the Computer Vision and Pattern Recognition Conference*, pages 10360–10371, 2025.

[72] Yuri Tolkach, Lisa Marie Wolgast, Alexander Damanakis, Alexey Pryalukhin, Simon Schallenberg, Wolfgang Hull, Marie-Lisa Eich, Wolfgang Schroeder, Anirban Mukhopadhyay, Moritz Fuchs, et al. Artificial intelligence for tumour tissue detection and histological regression grading in oesophageal adenocarcinomas: a retrospective algorithm development and validation study. *The Lancet Digital Health*, 5(5):e265–e275, 2023.

[73] Anurag Vaidya, Andrew Zhang, Guillaume Jaume, Andrew H. Song, Tong Ding, Sophia J. Wagner, Ming Y. Lu, Paul Doucet, Harry Robertson, Cristina Almagro-Perez, Richard J. Chen, Dina ElHarouni, Georges Ayoub, Connor Bossi, Keith L. Ligon, Georg Gerber, Long Phi Le, and Faisal Mahmood. Molecular-driven foundation model for oncologic pathology, 2025.

[74] Bastiaan S. Veeling, Jasper Linmans, Jim Winkens, Taco Cohen, and Max Welling. Rotation equivariant cnns for digital pathology. In Alejandro F. Frangi, Julia A. Schnabel, Christos Davatzikos, Carlos Alberola-López, and Gabor Fichtinger, editors, *Medical Image Computing and Computer Assisted Intervention – MICCAI 2018*, pages 210–218, Cham, 2018. Springer International Publishing.

[75] Ruchika Verma, Neeraj Kumar, Abhijeet Patil, Nikhil Cherian Kurian, Swapnil Rane, Simon Graham, Quoc Dang Vu, Mieke Zwager, Shan E. Ahmed Raza, Nasir Rajpoot, Xiyi Wu, Huai Chen, Yijie Huang, Lisheng Wang, Hyun Jung, G. Thomas Brown, Yanling Liu, Shuolin Liu, Seyed Alireza Fatemi Jahromi, Ali Asghar Khani, Ehsan Montahaei, Mahdieh Soleymani Baghshah, Hamid Behroozi, Pavel Semkin, Alexandre Rassadin, Prasad Dutande, Romil Lodaya, Ujjwal Baid, Bhakti Baheti, Sanjay Talbar, Amirreza Mahbod, Rupert Ecker, Isabella Ellinger, Zhipeng Luo, Bin Dong, Zhengyu Xu, Yuehan Yao, Shuai Lv, Ming Feng, Kele Xu, Hasib Zunair, Abdessamad Ben Hamza, Steven Smiley, Tang-Kai Yin, Qi-Rui Fang, Shikhar Srivastava, Dwarikanath Mahapatra, Lubomira Trnavska, Hanyun Zhang, Priya Lakshmi Narayanan, Justin Law, Yinyin Yuan, Abhiroop Tejomay, Aditya Mitkari, Dinesh Koka, Vikas Ramachandra, Lata Kini, and Amit Sethi. Monusac2020: A multi-organ nuclei segmentation and classification challenge. *IEEE Transactions on Medical Imaging*, 40(12):3413–3423, 2021.

[76] Eugene Vorontsov, George Shaikovski, Adam Casson, Julian Viret, Eric Zimmermann, Neil Tenenholz, Yi Kan Wang, Jan H. Bernhard, Ran A. Godrich, Juan A. Retamero, Jinru Shia, Mithat Gonen, Martin R. Weiser, David S. Klimstra, Razik Yousfi, Nicolo Fusi, Thomas J. Fuchs, Kristen Severson, and Siqi Liu. Prism2: Unlocking multi-modal general pathology ai with clinical dialogue, 2025.

[77] Xiyue Wang, Junhan Zhao, Eliana Marostica, Wei Yuan, Jietian Jin, Jiayu Zhang, Ruijiang Li, Hongping Tang, Kanran Wang, Yu Li, Fang Wang, Yulong Peng, Junyou Zhu, Jing Zhang, and Christopher. A pathology foundation model for cancer diagnosis and prognosis prediction. *Nature*, 634(8035):970–978, October 2024.

[78] Jerry Wei, Arief Suriawinata, Bing Ren, Xiaoying Liu, Mikhail Lisovsky, Louis Vaickus, Charles Brown, Michael Baker, Naofumi Tomita, Lorenzo Torresani, et al. A petri dish for histopathology image analysis. In *Artificial Intelligence in Medicine: 19th International Conference on Artificial Intelligence in Medicine, AIME 2021, Virtual Event, June 15–18, 2021, Proceedings*, pages 11–24. Springer, 2021.

[79] Hanwen Xu, Naoto Usuyama, Jaspreet Bagga, Sheng Zhang, Rajesh Rao, Tristan Naumann, Cliff Wong, Zelalem Gero, Javier González, Yu Gu, Yanbo Xu, Mu Wei, Wenhui Wang, Shuming Ma, Furu Wei, Jianwei Yang, Chunyuan Li, Jianfeng Gao, Jaylen Rosemon, Tucker Bower, Soohee Lee, Roshanthy Weerasinghe, Bill J. Wright, Ari Robicsek, Brian Piening, Carlo Bifulco, Sheng Wang, and Hoifung Poon. A whole-slide foundation model for digital pathology from real-world data. *Nature*, 630(8015):181–188, June 2024.

[80] Yingxue Xu, Yihui Wang, Fengtao Zhou, Jiabo Ma, Cheng Jin, Shu Yang, Jinbang Li, Zhengyu Zhang, Chenglong Zhao, Huajun Zhou, Zhenhui Li, Huangjing Lin, Xin Wang, Jiguang Wang, Anjia Han, Ronald Cheong Kin Chan, Li Liang, Xiuming Zhang, and Hao Chen. A multi-modal knowledge-enhanced whole-slide pathology foundation model. *Nature Communications*, 16:11406, 2025.

[81] Andrew Zhang, Guillaume Jaume, Anurag Vaidya, Tong Ding, and Faisal Mahmood. Accelerating data processing and benchmarking of ai models for pathology, 2025.

[82] Eric Zimmermann, Eugene Vorontsov, Julian Viret, Adam Casson, Michal Zelechowski, George Shaikovski, Neil Tenenholz, James Hall, Thomas Fuchs, Nicolo Fusi, Siqi Liu, and Kristen Severson. Virchow 2: Scaling Self-Supervised Mixed Magnification Models in Pathology, August 2024. arXiv:2408.00738.

A Appendix

A.1 Task Descriptions

HEST-Benchmark The HEST-Benchmark was introduced by [34] for benchmarking foundation models for histology on the task of gene expression prediction from H&E-stained images. The benchmark includes 72 spatial transcriptomics profiles (using Xenium or Visium technology) with corresponding H&E-stained images from 47 patients grouped into 10 tasks based on organ. Each task involves predicting the expression levels of the 50 most variable genes (highest normalized variance) from $112 \times 112 \mu\text{m}$ H&E-stained image patches (equivalent to 224×224 pixels at $20 \times$ magnification) centered on each spatial transcriptomics spot, formulated as a multivariate regression problem. We use the default Ridge Regression with PCA (256 factors) evaluation protocol to solve the multivariate regression problem for extracted embeddings [34]. Specifically, the objective of the 10 tasks is to predict gene expression levels for invasive ductal carcinoma (breast cancer, IDC), prostate adenocarcinoma (prostate cancer, PRAD), pancreatic adenocarcinoma (pancreatic cancer, PAAD), skin cutaneous melanoma (skin cancer, SKCM), colonic adenocarcinoma (colon cancer, COAD), rectal adenocarcinoma (rectum cancer, READ), clear cell renal cell carcinoma (kidney cancer, ccRCC), hepatocellular carcinoma (liver cancer, HCC), lung adenocarcinoma (lung cancer, LUAD), and axillary lymph nodes in IDC (metastatic, LYMPH-IDC). The benchmark applies patient-stratified splits to avoid any train/test patient-level data leakage, resulting in a k-fold cross-validation where k is the number of patients [34]. Performance is measured as the Pearson correlation coefficient between the predicted and measured gene expression. Results are reported as the mean across folds.

BACH The BACH dataset comprises 400 H&E microscopy images (2048×1536 pixels at $20 \times$ magnification) of breast cancer biopsies. It was introduced as part of the ICIAR 2018 Grand Challenge on BreAst Cancer Histology images (BACH) [3]. The task of the challenge is to classify each image into one of the following four classes: “normal”, “benign”, “in situ carcinoma”, and “invasive carcinoma”. The dataset is split into 268 training images (67 images per class) and 132 test images (33 images per class). The patches are resized and cropped to 224×224 pixels.

CRC-100k The CRC-100k dataset contains 107,180 H&E images (224×224 pixels at $20 \times$ magnification) extracted from colorectal cancer (CRC) tissue samples [41]. The tissue samples originate from CRC primary tumors and CRC liver metastases. The task of this benchmark is to classify each image into one of the following 9 tissue classes: “adipose”, “background”, “debris”, “lymphocytes”, “mucus”, “smooth muscle”, “normal colon mucosa”, “cancer-associated stroma”, and “colorectal adenocarcinoma epithelium”. The dataset is split into 100,000 training images (NCT-CRC-HE-100K-NONORM) and 7,180 test images (CRC-VAL-HE-7K). We use the original (no-norm) images without Macenko color normalization [40].

MHIST The task of MHIST is to classify images of colorectal polyps into hyperplastic polyps (HPs) vs. sessile serrated adenomas (SSAs) [78]. This distinction is clinically important as HPs are typically benign whereas SSAs are precancerous lesions that can turn into cancer if left untreated. The task is challenging for pathologists, often showing considerable inter-pathologist variability. The MHIST dataset consists of 3,152 H&E images (224×224 pixels at $8 \times$ magnification) of colorectal polyps. Labels are derived from the majority vote of seven pathologists. The dataset is split into 2,162 training images (1,545 HP and 617 SSA) and 990 test images (630 HP and 360 SSA).

PCAM PCAM (PatchCamelyon) defines the clinically-relevant task of metastasis detection as a binary image classification task [74]. The dataset consists of 327,680 H&E images (96×96 pixels at $10 \times$ magnification) extracted from scans of sentinel lymph node sections. Each image is annotated with a binary label indicating the presence of metastatic breast cancer tissue. An image is labeled as metastatic if the center (32×32 pixels) region contains at least one pixel of tumor tissue. The dataset is split by ratios of 80:10:10 into training, validation, and test sets with no overlap of WSIs/cases between the splits. Moreover, every split has a 50:50 balance of positive and negative examples. For evaluation, we resize each image to 224×224 pixels. PCAM has been derived from the CAMELYON16 Challenge [5].

CAMELYON16 The task of the CAMELYON16 challenge [5] is to classify whole slide images (WSIs) of lymph node tissue sections into metastatic breast cancer tissue being present or not. The

dataset comprises 399 H&E-stained WSIs of sentinel lymph node sections, which were acquired and scanned ($40\times$ magnification) at two centers from the Netherlands [5]. The dataset is split into 270 training slides (110 with and 160 without metastasis) and 129 test slides (49 with and 80 without metastasis). Here, we report results for the CAMELYON16 (small) setup in *eva* [27], which randomly samples max. 1,000 patches per slide.

PANDA The PANDA challenge [9] is concerned with the challenging task of tumor grading of whole slide images (WSIs) of prostate cancer biopsies, which suffers from significant inter-observer variability between pathologists. Prostate cancer grading follows the Gleason grading system (3, 4, or 5) based on architectural growth patterns of the tumor, which are then converted into an ISUP grade on a scale of 1–5 for usage as a prognostic marker. The dataset features 9,555 H&E-stained WSIs (subset with noisy labels removed) of prostate tissue biopsies from two medical centers scanned at $20\times$ magnification. Specifically, the task is to classify each WSI into an ISUP grade of 0–5 (six classes), where 0 means that a biopsy does not contain any cancer. The dataset is split into 6,686 training slides, 1,430 validation slides, and 1,439 test slides in a class-stratified manner. Here, we report results for the PANDA (small) setup in *eva* [27], which considers a fewer number of total slides (955 train, 477 validation, 477 test) and fewer randomly sampled patches per slide (200).

BreakHis The Breast Cancer Histopathological Image Classification (BreakHis) dataset was introduced for the task of classifying breast tumor tissue into benign and malignant histological subtypes [70]. The task involves multi-class classification of microscopic images into eight categories: “adenosis” (A, benign), “fibroadenoma” (F, benign), “phyllodes tumor” (PT, benign), “tubular adenoma” (TA), “carcinoma” (DC, malignant), “lobular carcinoma” (LC, malignant), “mucinous carcinoma” (MC, malignant) and “papillary carcinoma” (PC, malignant). The original dataset consists of 9,109 microscopic images collected from 82 patients at multiple magnification factors, $40\times$, $100\times$, $200\times$, and $400\times$. For this benchmark, we follow the *eva* [27] evaluation protocol and use only the $40\times$ magnification subset, which consists of 1,995 H&E-stained images (700×460 pixels at $40\times$ magnification, $0.49\text{ }\mu\text{m/pixel}$) selected from classes with at least 7 patients to ensure statistical robustness: TA, MC, F & DC. The dataset is split using patient-stratified partitioning, resulting in 1,132 training images and 339 validation images with approximate class balance maintained across splits.

CoNSeP The CoNSeP (Colorectal Nuclear Segmentation and Phenotypes) dataset was introduced for the task of nuclear segmentation and classification in colorectal tissue [28]. The task involves segmenting and classifying cell nuclei into four categories: “miscellaneous”, “inflammatory”, “epithelial” (combining normal and malignant/dysplastic epithelial cells), and “spindle-shaped” (combining fibroblast, muscle, and endothelial cells). The dataset consists of 41 H&E-stained images ($1,000\times1,000$ pixels at $40\times$ magnification) extracted from 16 whole-slide images of unique colorectal cancer patients, containing 24,319 annotated nuclei in total. Segmentation masks are provided as instance-level annotations indicating both the spatial extent and class label of each nucleus. The dataset is split into 27 training images and 14 test images. Following the *eva* [27] protocol, we use the test split as the validation split.

Gleason Arvaniti The Gleason Arvaniti dataset was introduced for automated Gleason grading of prostate cancer tissue microarrays (TMAs) [4]. The task involves multi-class classification of prostate tissue images into four categories: “benign”, “Gleason pattern 3”, “Gleason pattern 4”, and “Gleason pattern 5”. The dataset comprises 22,752 H&E-stained images (750×750 pixels at $40\times$ magnification) from 886 patients across two cohorts: a training cohort of 641 patients and an independent test cohort of 245 patients, with annotations provided by two experienced pathologists. Following the *eva* [27] protocol, the dataset is split into 15,303 training images, 2,482 validation images selected from TMA 76 due to its balanced distribution of Gleason scores, and 4,967 test images.

MoNuSAC The MoNuSAC (Multi-Organ Nuclei Segmentation and Classification Challenge) dataset was introduced for the task of nuclear segmentation and classification across multiple organs and tissue types [75]. The task involves segmenting and classifying cell nuclei into five categories: “epithelial cells”, “lymphocytes”, “macrophages”, “neutrophils”, and “ambiguous” (cells that cannot be definitively classified into the other categories). The dataset consists of 294 H&E-stained tissue images from four organs: breast, kidney, lung, and prostate, with variable dimensions, from 113×81

to $1,398 \times 1,956$ pixels at $40 \times$ magnification. The images were collected from 37 hospitals and 71 patients, containing over 46,000 annotated nuclei. Instance-level segmentation masks are provided, indicating both the spatial extent and class label of each nucleus. The dataset is split into 209 training images and 85 test images. Following the *eva* [27] evaluation protocol, we use the test split as the validation split.

MSI CRC (patch) This dataset contains 173,630 H&E images (224×224 pixels at $20 \times$ magnification) extracted from $N = 360$ colorectal cancer (CRC) tissue scans from TCGA (TCGA-CRC-DX). The task is binary classification of microsatellite instability (MSI) vs. microsatellite stability (MSS), which is a clinically important prognostic marker [42, 36]. The dataset is split into 56,044 (28,022 MSI + 28,022 MSS) training images, 18,682 (9,341 MSI + 9,341 MSS) validation images, and 98,904 (28,335 MSI + 70,569 MSS) test images.

MSI STAD (patch) This dataset contains 198,464 H&E images (224×224 pixels at $20 \times$ magnification) extracted from $N = 315$ stomach adenocarcinoma (STAD) tissue scans from TCGA (TCGA-STAD). The task is binary classification of microsatellite instability (MSI) vs. microsatellite stability (MSS), which is a clinically important prognostic marker [42, 36]. The dataset is split into 60,342 (30,171 MSI + 30,171 MSS) training images, 20,114 (10,057 MSI + 10,057 MSS) validation images, and 118,008 (27,904 MSI + 90,104 MSS) test images.

TCGA Uniform (10 \times) and (20 \times) The TCGA Uniform dataset [47] contains 264,110 to 271,700 patches per resolution with 256×256 pixels. The task is to differentiate between 32 cancer classes from different tissue types (e.g., Colon adenocarcinoma). Only patches showing the specific cancer type were extracted from the TCGA WSIs based on annotations from two trained pathologists. As there is no official train and test split, we generate five folds with no overlapping patients and sampled 100 patches per class and fold, resulting in a total dataset size of 16,000 patches. We generate one dataset containing patches with $0.5 \mu\text{m}/\text{pixel}$ (20 \times) and one with $1.0 \mu\text{m}/\text{pixel}$ (10 \times) to test the performance of the foundation models at different zoom levels. The results represent the mean balanced accuracy for the five-fold cross-validation evaluation.

PathoROB The PathoROB Robustness Index was introduced by [48] as a novel metric to quantify the robustness of pathology foundation models to non-biological confounding features, specifically medical center differences arising from variations in staining procedures, scanner hardware, surgical techniques, and laboratory protocols. The Robustness Index measures the degree to which biological features (e.g., tissue type, cancer type) dominate over confounding non-biological features (e.g., medical center signatures) in the neighborhood structure of a foundation model’s embedding space. The benchmark comprises three datasets sourced from CAMELYON[5, 10], TCGA[47], and Tolkach ESCA[72], covering 28 biological classes from 34 medical centers.

Plismbench The Plismbench robustness benchmark was introduced by [22] as a framework to quantify the robustness of pathology foundation models to technical variations arising from different scanning devices and staining procedures. The benchmark measures robustness through cosine similarity and top-k retrieval accuracy metrics, evaluating the ability of foundation models to maintain consistent representations of matching tissue tiles across different technical conditions. The evaluation is performed on registered tile pairs from the PLISM dataset [58], which consists of 46 human tissue types processed with 13 different H&E staining conditions and captured using 7 WSI scanners, resulting in 16,278 registered tissue tile pairs. Robustness is assessed across three conditions: cross-scanner robustness (fixed staining), cross-staining robustness (fixed scanner), and combined cross-scanner and cross-staining robustness.

Patho-Bench The Patho-Bench framework was introduced by [81] for comprehensive benchmarking of patch-level and slide-level foundation models for whole-slide images (WSIs) across diverse clinically relevant pathology tasks. The benchmark comprises 95 tasks, subcategorized into seven clinical prediction categories: morphological subtyping (11 tasks), tissue microenvironment (TME) characterization (16 tasks), tumor grading (9 tasks), molecular subtyping (6 tasks), mutation prediction (34 tasks), treatment response and assessment (7 tasks), and survival prediction (12 tasks). We evaluate on a subset of 53 tasks drawn from multiple datasets, including CPTAC datasets covering breast (BRCA), colorectal (COAD), glioblastoma (GBM), head and neck (HNSC), lung squamous and adenocarcinoma (LSSC, LUAD), pancreatic (PDA), clear cell renal cell carcinoma

(ccRCC), BC-Therapy for breast cancer, MBC for metastatic breast cancer, Hancock for head and neck squamous cell carcinoma, IMP-Cervical for cervical cancer, and Boehmke for ovarian cancer. Each task is formulated as a WSI-level classification or survival prediction problem. Following the Patho-Bench [81] evaluation protocol, we use the Attention-based Multiple Instance Learning (ABMIL) framework [33], where H&E-stained whole-slide images are represented as bags of patch-level feature embeddings extracted from foundation models. We employ the pre-defined task folds, depending on cohort size with label- and patient-stratified splits.

A.2 Additional results

	Atlas 2	Pluto-4G*	Atlas	UNI2-H	H-Optimus-0	Midnight-12k	Virchow2	Prov-GigaPath	UNI	Plukon v2	H-Optimus-1*
HEST-ccRCC	26.0	28.9	<u>27.8</u>	26.4	26.8	21.3	27.4	24.7	24.0	26.6	24.5
HEST-COAD	32.3	31.6	25.9	30.1	30.9	29.1	25.9	30.2	26.2	25.0	<u>32.0</u>
HEST-IDC	62.1	<u>60.6</u>	59.6	59.0	59.8	58.2	59.2	56.5	57.4	54.1	60.2
HEST-LUNG	<u>57.2</u>	56.9	57.0	55.8	55.9	55.8	55.3	54.2	54.6	54.2	57.8
HEST-LYMPH-IDC	28.2	27.3	25.7	27.2	25.9	26.4	25.6	25.1	25.6	24.4	<u>27.7</u>
HEST-PAAD	52.3	<u>51.1</u>	50.7	50.0	49.1	49.0	47.2	48.6	48.1	44.5	49.6
HEST-PRAD	38.5	37.4	35.3	35.7	38.5	33.7	34.8	37.0	29.4	35.5	<u>37.8</u>
HEST-RECTUM	<u>24.0</u>	23.3	21.3	22.3	22.2	18.5	20.9	19.5	18.4	17.5	24.2
HEST-SKCM	67.8	<u>67.0</u>	56.2	65.9	64.5	63.6	61.9	57.6	63.5	55.5	65.9
MSI CRC (patch)	78.2	-	71.7	<u>71.8</u>	69.7	69.9	71.6	69.0	69.1	67.6	-
MSI STAD (patch)	75.8	-	<u>73.5</u>	72.8	72.6	72.6	73.0	67.5	68.6	68.6	-
HEST-Average	43.2	<u>42.7</u>	39.9	41.4	41.5	39.5	39.8	39.3	38.6	37.5	42.2
Molecular-Average	49.3	-	45.9	<u>47.0</u>	46.9	45.3	45.7	44.5	44.1	43.0	-
<hr/>											
BACH	91.1	93.8	<u>93.0</u>	91.5	75.9	90.5	88.3	75.5	78.5	73.3	-
BreakHis	<u>85.6</u>	81.5	91.1	85.5	80.1	81.2	82.1	82.8	78.9	71.3	-
CoNSeP	66.1	65.0	<u>65.1</u>	63.6	64.5	62.4	64.5	63.0	63.0	62.9	-
CRC-100k	97.1	96.4	<u>96.9</u>	96.5	95.5	96.6	96.7	95.1	94.4	93.9	95.6
Gleason	<u>79.5</u>	79.3	78.7	77.5	77.0	80.0	78.3	72.4	75.0	75.7	-
MHIST	88.0	<u>87.5</u>	86.1	82.6	84.4	80.4	86.1	83.0	84.4	77.7	83.5
MoNuSAC	69.4	70.4	67.4	64.5	68.1	65.8	66.8	66.4	65.0	64.3	-
PANDA	68.3	66.8	65.8	64.6	<u>67.2</u>	65.2	64.9	65.5	65.1	62.4	-
PCAM	96.1	95.1	<u>95.3</u>	95.0	94.3	92.9	93.8	94.5	93.7	89.4	-
CAMELYON16 (0.25 MPP)	86.5	-	85.5	85.2	83.1	84.0	<u>85.9</u>	81.0	83.2	80.2	-
TCGA Uniform (1.0 MPP)	84.2	-	78.7	79.3	75.6	<u>82.7</u>	78.2	74.3	74.0	69.8	-
TCGA Uniform (0.5 MPP)	82.6	-	76.8	78.8	78.7	<u>82.5</u>	77.8	74.0	74.5	76.7	-
Morphology-Average-Pluto-4G	82.4	81.8	<u>82.2</u>	80.1	78.6	79.4	80.2	77.6	77.6	74.5	-
Morphology-Average	82.9	-	<u>81.7</u>	80.4	78.7	80.4	80.3	77.3	77.5	74.8	-
<hr/>											
Prediction-Average-Pluto-4G	62.8	<u>62.2</u>	61.0	60.8	60.0	59.5	60.0	58.4	58.1	56.0	-
Prediction-Average	66.8	-	<u>64.6</u>	64.4	63.5	63.6	63.7	61.6	61.5	59.6	-
<hr/>											
Robustness Index (Camelyon)	93.6	-	<u>80.0</u>	51.5	69.0	46.7	74.1	36.0	10.8	1.6	-
Robustness Index (TCGA)	87.8	-	<u>82.3</u>	79.6	80.4	<u>85.4</u>	82.7	72.7	72.9	58.8	-
Robustness Index (Tolkach)	95.9	-	93.2	91.4	91.0	<u>93.9</u>	95.2	68.9	87.6	73.3	-
Plismbench (Leaderboard metric)	60.5	-	35.4	33.2	<u>48.0</u>	33.8	44.8	33.3	32.5	16.4	-
Robustness-Average	84.4	-	72.7	63.9	72.1	65.0	<u>74.2</u>	52.7	51.0	37.5	-

*Results for Pluto-4G taken from [60]. Results for H-Optimus-1 taken from [8].

Table 4: Same table content and formatting as in Table 1, but for the CLS token instead of CLS+MEAN.

	Atlas 2	ViT-B					ViT-S				
		Atlas 2-B	ViT-B/8 [1]	Hilbou-B	Phnikon	H0-mini*	Atlas 2-S	Pluto-4S-8*	Pluto-4S-16*	ViTS/8 [37]	ViTS/8 [1]
HEST-ccRCC	26.0	<u>24.9</u>	23.1	20.6	24.2	26.7	<u>24.0</u>	-	-	25.5	23.5
HEST-COAD	32.3	31.8	<u>26.8</u>	25.9	26.2	24.9	<u>27.0</u>	-	-	27.6	22.8
HEST-IDC	62.1	60.1	56.0	54.8	53.3	<u>58.6</u>	58.4	-	-	<u>54.8</u>	53.0
HEST-LUNG	57.2	56.1	51.8	54.1	54.7	<u>54.8</u>	55.4	-	-	<u>54.1</u>	50.5
HEST-LYMPH-IDC	28.2	26.3	22.7	<u>23.7</u>	<u>23.7</u>	26.3	24.8	-	-	25.4	24.6
HEST-PAAD	52.3	50.1	46.0	46.1	44.2	<u>49.2</u>	45.8	-	-	<u>42.2</u>	41.8
HEST-PRAD	38.5	37.3	36.1	29.7	34.2	<u>36.8</u>	38.3	-	-	25.0	<u>33.4</u>
HEST-RECTUM	24.0	22.1	16.2	16.4	15.3	<u>18.6</u>	15.4	-	-	<u>14.9</u>	14.7
HEST-SKCM	67.8	63.0	57.3	54.4	53.6	<u>60.1</u>	60.1	-	-	<u>58.1</u>	51.8
MSI CRC (patch)	78.2	74.4	<u>68.6</u>	68.0	67.4	-	<u>70.8</u>	-	-	71.0	68.4
MSI STAD (patch)	75.8	75.5	68.7	<u>70.2</u>	67.3	-	<u>76.6</u>	-	-	<u>72.4</u>	70.4
HEST-Average	43.2	41.3	37.3	36.2	36.6	<u>39.6</u>	38.8	<u>36.5</u>	36.2	36.4	35.1
Molecular-Average	49.3	47.4	<u>43.0</u>	42.2	42.2	-	45.1	-	-	<u>42.8</u>	41.4
<hr/>											
BACH	91.1	89.4	<u>86.6</u>	82.5	73.0	77.4	90.6	<u>82.7</u>	79.6	76.3	81.7
BreakHis	85.6	84.8	<u>83.2</u>	74.1	70.8	-	87.1	<u>81.3</u>	79.2	68.8	71.7
CoNSeP	66.1	66.2	<u>64.5</u>	63.3	62.8	62.9	65.2	<u>64.9</u>	62.1	63.4	63.9
CRC-100k	97.1	96.9	95.6	95.1	94.0	<u>96.1</u>	96.7	<u>95.2</u>	95.0	94.5	<u>95.2</u>
Gleason	79.5	79.2	<u>74.4</u>	72.9	72.9	-	77.0	<u>76.2</u>	<u>76.3</u>	74.4	71.7
MHIST	88.0	86.0	<u>82.9</u>	79.0	80.3	79.0	83.8	<u>83.7</u>	83.5	74.8	81.8
MoNuSAC	69.4	69.2	<u>68.5</u>	64.9	64.3	64.3	68.9	<u>67.8</u>	64.0	66.7	65.3
PANDA	68.3	68.5	63.4	62.4	64.5	<u>66.7</u>	65.2	61.8	61.5	<u>61.9</u>	60.4
PCAM	96.1	94.7	91.5	<u>94.5</u>	92.0	94.2	93.8	90.7	90.9	<u>92.0</u>	88.6
CAMELYON16 (0.25 MPP)	86.5	85.1	81.8	<u>77.1</u>	81.2	<u>84.2</u>	85.7	-	-	78.4	<u>80.3</u>
TCGA Uniform (1.0 MPP)	84.2	<u>79.8</u>	80.3	72.2	70.5	-	74.4	-	-	71.6	<u>73.8</u>
TCGA Uniform (0.5 MPP)	82.6	<u>78.1</u>	79.3	70.5	75.5	-	72.3	-	-	71.3	<u>71.6</u>
Morphology-Average-Pluto-4G	82.4	81.7	<u>79.0</u>	76.5	75.0	-	80.9	<u>78.3</u>	76.9	74.8	75.6
Morphology-Average	82.9	81.5	<u>79.3</u>	75.7	75.2	-	80.1	-	-	74.5	<u>75.5</u>
<hr/>											
Prediction-Average-Pluto-4G	62.8	61.5	<u>58.1</u>	56.4	55.8	-	59.9	<u>57.4</u>	56.6	55.6	55.4
Prediction-Average	66.8	65.2	<u>62.0</u>	59.7	59.4	-	63.4	-	-	<u>59.4</u>	59.2
<hr/>											
Robustness Index (Camelyon)	93.6	87.7	<u>13.2</u>	4.8	0.9	-	83.8	-	-	3.6	<u>29.6</u>
Robustness Index (TCGA)	87.8	82.8	<u>75.9</u>	59.7	60.0	-	79.9	-	-	65.8	<u>74.6</u>
Robustness Index (Tolkach)	95.9	95.2	<u>88.8</u>	75.5	76.1	-	95.7	-	-	82.3	<u>92.2</u>
Plismbench (Leaderboard metric)	60.5	63.9	32.6	20.4	19.3	<u>54.1</u>	65.8	-	-	30.0	<u>36.3</u>
Robustness-Average	84.4	82.4	<u>52.6</u>	40.1	39.1	-	81.3	-	-	45.4	<u>58.2</u>

*Results for H0-mini taken from [22] (eva), [63] (Plismbench) and [30] (HEST). Results for Pluto-4S-8 and Pluto-4S-16 taken from [60].

Table 5: Same table content and formatting as in Table 3, but for the CLS token instead of CLS+MEAN.

	Alles ^{2-B}		Alles ^{3-B}		Pluto-4G*		Alles ^{2-S}		Alles ^{3-S}		VTF-B/8/11		Pro-GigaPape		VTF-B/16/12		HODimun-0		VTF-B/8/11		Pluto-4S-8*		VTF-B/16/16		Pluto-4S-16*		VTF-S/8/11		VTF-S/8/13/11		VTF-S/16/11		VTF-S/16/13/11		VTF-S/16/16*		H0 mini*	
HEST-ccRCC	27.9	26.0	24.8	-	29.5	28.1	20.9	27.2	24.9	25.1	-	22.8	23.4	27.4	-	24.2	26.7	25.7	-	23.7	26.1	26.4	-	25.7	27.6	27.0	-	27.8	30.2	23.0	24.3	27.6	27.0	27.0				
HEST-COAD	34.9	32.4	27.9	-	29.3	30.2	31.8	25.8	32.0	30.2	25.8	-	28.7	28.0	25.6	-	27.8	30.2	23.0	24.3	27.6	27.0	27.0	-	27.8	30.2	23.0	24.3	27.6	27.0	27.0							
HEST-IDC	62.7	60.8	58.9	-	60.4	60.5	61.1	59.9	59.7	58.1	57.0	58.5	-	56.0	55.7	56.8	-	54.8	55.2	54.5	54.0	53.1	59.1	-	54.5	55.2	54.0	53.1	54.0	53.1	59.1							
HEST-LUNG	59.4	56.6	56.4	-	58.1	57.4	57.5	58.3	56.8	56.1	53.9	55.6	-	54.9	53.5	55.0	-	56.7	54.4	54.4	53.2	53.7	52.2	56.3	-	53.7	52.2	53.7	52.2	53.7	52.2	56.3						
HEST-LYMPH-IDC	28.6	26.6	25.2	-	26.2	27.4	26.6	27.5	25.5	25.8	25.0	23.5	25.8	-	25.0	23.7	24.8	-	23.8	24.9	23.9	23.0	23.0	23.0	23.0	-	23.0	23.0	23.0	23.0	23.0	23.0	23.0					
HEST-PAAD	54.2	52.3	46.6	-	51.7	52.3	51.1	50.2	47.8	49.9	47.8	48.8	-	45.9	46.2	47.7	-	46.5	44.2	43.3	44.7	44.4	50.7	-	44.4	44.7	44.4	44.4	44.4	44.4	44.4							
HEST-PRAD	39.7	38.1	36.9	-	38.6	37.5	37.5	36.2	37.1	35.3	39.1	38.0	32.7	-	30.6	32.5	37.9	-	34.5	27.1	34.4	33.4	33.4	36.3	-	36.3	33.4	33.4	33.4	33.4	33.4	33.4						
HEST-RECTUM	25.4	22.2	16.8	-	22.6	22.7	24.0	20.7	20.7	19.4	17.0	17.6	-	17.6	15.5	18.7	-	16.6	14.4	14.5	13.8	13.8	20.5	-	20.5	14.5	14.5	14.5	14.5	14.5	14.5	14.5						
HEST-SKCM	70.0	65.1	60.8	-	62.0	68.3	66.1	64.8	64.0	59.7	59.4	62.3	-	55.9	55.5	58.4	-	54.5	57.5	56.5	53.9	54.9	61.2	-	61.2	54.9	54.9	54.9	54.9	54.9	54.9	54.9						
MSICRC (patch)	78.0	75.4	70.8	-	72.6	72.0	70.0	70.8	71.9	69.5	68.8	69.7	-	68.3	68.0	68.3	-	67.2	70.2	69.4	68.1	69.6	-	-	69.6	68.1	68.1	68.1	68.1	68.1	68.1							
MSISTAD (patch)	76.1	74.3	76.0	-	73.0	73.1	72.2	73.7	72.5	68.1	68.1	68.6	-	71.0	68.9	69.2	-	67.1	72.6	72.3	70.1	68.7	-	-	68.7	70.1	70.1	70.1	70.1	70.1	70.1							
HEST-Average	44.8	42.2	39.4	-	43.2	42.0	43.0	42.5	41.2	40.3	40.5	39.1	39.1	36.9	37.5	37.1	39.1	36.4	37.7	37.3	36.5	36.1	40.4	-	40.4	36.1	36.1	36.1	36.1	36.1	36.1	36.1						
Molecular-Average	50.6	48.2	45.6	-	47.6	47.6	48.4	47.7	46.8	46.1	45.6	44.4	44.6	-	43.3	42.8	44.5	-	43.1	43.5	42.8	42.1	42.1	-	-	42.1	42.1	42.1	42.1	42.1	42.1	42.1						
BACH	91.7	90.0	90.1	93.2	92.3	92.2	74.7	90.6	88.6	79.2	88.0	79.7	85.1	81.9	83.0	73.6	79.8	73.5	77.3	77.3	80.2	84.1	77.7	-	77.7	80.2	80.2	80.2	80.2	80.2	80.2	80.2	80.2	80.2	80.2			
BreakHis	88.3	81.3	86.6	81.8	86.3	81.0	83.1	81.1	84.5	84.4	80.4	84.4	80.8	82.5	79.8	82.5	79.8	79.8	79.8	79.8	79.8	79.8	79.8	-	79.8	79.8	79.8	79.8	79.8	79.8	79.8	79.8	79.8	79.8	-			
CohNSep	66.1	62.2	65.2	65.0	65.1	63.6	64.5	63.4	64.5	63.0	64.5	63.0	64.9	63.3	60.6	62.9	62.1	62.8	63.4	63.9	60.3	60.0	62.9	-	62.9	63.9	63.9	63.9	63.9	63.9	63.9	63.9	63.9	63.9	-			
CRC-100k	97.2	97.0	96.8	96.9	96.9	96.8	96.9	96.4	96.7	96.6	95.9	96.0	96.1	95.4	95.8	95.9	95.3	95.5	94.7	94.9	94.5	94.0	-	-	94.0	94.5	94.5	94.5	94.5	94.5	94.5	94.5	94.5	94.5	-			
Gleason	80.7	79.4	77.1	78.4	77.6	77.3	79.0	78.5	78.4	77.6	75.4	76.0	76.3	74.1	75.3	76.6	74.2	74.3	74.3	74.3	74.3	74.3	74.3	-	74.3	74.3	74.3	74.3	74.3	74.3	74.3	74.3	74.3	74.3	-			
MHIST	88.5	86.9	84.9	87.9	86.8	82.6	85.1	81.2	86.5	82.6	83.0	83.3	84.2	79.9	84.3	79.6	83.4	82.3	82.3	82.3	82.3	82.3	82.3	-	82.3	82.3	82.3	82.3	82.3	82.3	82.3	82.3	82.3	82.3	-			
MoNuSAC	69.4	69.2	68.9	70.4	67.4	64.5	68.1	65.8	66.8	66.4	68.5	65.0	67.8	64.9	63.5	64.0	64.0	64.3	64.3	64.3	64.3	64.3	64.3	-	64.3	64.3	64.3	64.3	64.3	64.3	64.3	64.3	64.3	64.3	-			
PANDA	68.3	68.7	66.3	66.6	66.4	66.2	65.4	64.7	65.0	64.7	65.0	64.7	65.4	63.1	63.2	62.5	62.1	63.0	64.5	61.9	60.3	60.4	-	60.4	60.3	60.3	60.3	60.3	60.3	60.3	60.3	60.3	60.3	-				
PCAM	96.1	94.7	93.9	95.2	93.9	95.2	94.4	95.1	94.4	94.6	92.0	93.9	91.4	94.3	90.9	90.0	91.6	92.8	92.4	88.6	90.5	90.2	-	90.2	90.5	90.5	90.5	90.5	90.5	90.5	90.5	90.5	90.5	-				
CAMELYON16 (0.25 MPP)	86.8	85.4	84.7	-	86.3	85.9	84.7	86.1	85.7	80.7	81.9	84.1	-	80.3	80.8	80.7	-	82.8	79.1	81.1	80.0	80.7	79.4	-	79.4	80.7	80.7	80.7	80.7	80.7	80.7	80.7	80.7	80.7	-			
TCGA Uniform (1.0 MPP)	84.1	80.0	74.7	-	78.7	79.4	76.0	83.7	78.0	74.7	80.5	74.3	-	72.4	78.1	70.1	-	75.6	71.5	72.2	75.4	75.4	75.4	-	75.4	75.4	75.4	75.4	75.4	75.4	75.4	75.4	75.4	75.4	-			
TCGA Uniform (0.5 MPP)	82.7	78.1	72.3	-	77.0	78.8	78.8	83.2	77.5	74.3	79.2	74.5	-	71.1	77.5	76.7	-	75.6	71.5	72.2	75.4	75.4	75.4	-	75.4	75.4	75.4	75.4	75.4	75.4	75.4	75.4	75.4	75.4	-			
Morphology-Average-Pluto-4G	82.9	81.5	81.1	81.7	82.0	80.6	78.6	79.7	80.1	78.3	79.6	78.1	-	78.8	77.4	77.5	74.9	77.0	75.6	75.6	75.6	75.6	75.6	-	75.6	75.6	75.6	75.6	75.6	75.6	75.6	75.6	75.6	75.6	-			
Morphology-Average	83.3	81.4	80.1	-	81.7	80.8	78.9	80.9	80.2	77.9	79.8	78.0	-	76.7	77.8	75.1	-	75.8	75.2	75.8	75.8	75.8	75.8	-	75.8	75.8	75.8	75.8	75.8	75.8	75.8	75.8	75.8	75.8	-			
Prediction-Average-Pluto-4G	63.8	61.9	60.2	62.5	62.0	61.8	60.6	60.5	60.2	59.4	59.3	58.6	-	57.8	57.4	57.3	57.0	56.7	56.6	56.4	56.2	56.1	55.6	-	55.6	56.1	56.1	56.1	56.1	56.1	56.1	56.1	56.1	56.1	-			
Prediction-Average	67.7	65.5	63.6	-	65.4	65.3	64.0	64.6	63.9	62.4	62.9	62.0	-	60.7	61.1	60.5	-	60.1	60.0	60.0	60.0	60.0	60.0	-	60.0	60.0	60.0	60.0	60.0	60.0	60.0	60.0	60.0	60.0	-			

Table 6: Prediction results for tasks with morphology and molecular targets as well as for robustness benchmarks. The table shows results for all models from Table 1&3, as well as for additional resource efficient models that use a patch-token size of 16. The **best** result per row is in bold, the second best result is underlined. *Results for H0-mini taken from [22] (HEST, eva) and [62] (PathoROB). Results for Pluto-4G, Pluto-4S-8 and Pluto-4S-16 taken from [60].

Prediction-Average-Pluto-4G		Prediction-Average		Prediction-Average-Pluto-4G		Prediction-Average	
HEST- ¹ -GRCC	26.0	24.9	24.0	28.9	27.8	26.4	26.8
HEST- ¹ -COAD	<u>32.3</u>	31.8	27.0	31.6	25.9	30.1	30.9
HEST- ¹ -DC	<u>62.1</u>	60.1	58.4	60.6	59.6	59.0	59.8
HEST- ¹ -LUNG	<u>57.2</u>	56.1	55.4	56.9	57.0	55.8	55.9
HEST- ¹ -LYMPH-1DC	<u>28.2</u>	26.3	24.8	27.3	25.7	27.2	25.9
HEST- ¹ -PAAD	<u>52.3</u>	50.1	45.8	51.1	50.7	50.0	49.1
HEST- ¹ -PRAD	<u>38.5</u>	37.3	38.3	37.4	35.3	35.7	38.5
HEST- ¹ -RECTUM	<u>24.0</u>	22.1	15.4	23.3	22.3	18.2	18.5
HEST- ¹ -SKCM	<u>67.8</u>	63.0	60.1	<u>67.0</u>	56.2	65.9	64.5
MSI-CRC (patch)	<u>78.2</u>	74.4	70.8	-	71.7	71.8	69.7
MSI-STAD (patch)	<u>75.8</u>	<u>76.6</u>	-	73.5	72.8	72.6	73.0
HEST-Average	<u>43.2</u>	41.3	38.8	<u>42.7</u>	39.9	41.4	41.5
Molecular-Average	<u>49.3</u>	<u>47.4</u>	45.1	-	45.9	47.0	46.9
Alphas- ² -B							
Alphas- ² -S	<u>49.3</u>	<u>47.4</u>	45.1	-	45.9	47.0	46.9
Alphas- ² -A							
Alphas- ² -H	<u>49.3</u>	<u>47.4</u>	45.1	-	45.9	47.0	46.9
DIN2-H							
DIN2-H	<u>49.3</u>	<u>47.4</u>	45.1	-	45.9	47.0	46.9
H2Optimus-0							
H2Optimus-0	<u>49.3</u>	<u>47.4</u>	45.1	-	45.9	47.0	46.9
H2Optimus-1							
H2Optimus-1	<u>49.3</u>	<u>47.4</u>	45.1	-	45.9	47.0	46.9
H2Optimus-2							
H2Optimus-2	<u>49.3</u>	<u>47.4</u>	45.1	-	45.9	47.0	46.9
H2Optimus-3							
H2Optimus-3	<u>49.3</u>	<u>47.4</u>	45.1	-	45.9	47.0	46.9
H2Optimus-4							
H2Optimus-4	<u>49.3</u>	<u>47.4</u>	45.1	-	45.9	47.0	46.9
H2Optimus-5							
H2Optimus-5	<u>49.3</u>	<u>47.4</u>	45.1	-	45.9	47.0	46.9
H2Optimus-6							
H2Optimus-6	<u>49.3</u>	<u>47.4</u>	45.1	-	45.9	47.0	46.9
H2Optimus-7							
H2Optimus-7	<u>49.3</u>	<u>47.4</u>	45.1	-	45.9	47.0	46.9
H2Optimus-8							
H2Optimus-8	<u>49.3</u>	<u>47.4</u>	45.1	-	45.9	47.0	46.9
H2Optimus-9							
H2Optimus-9	<u>49.3</u>	<u>47.4</u>	45.1	-	45.9	47.0	46.9
H2Optimus-10							
H2Optimus-10	<u>49.3</u>	<u>47.4</u>	45.1	-	45.9	47.0	46.9
H2Optimus-11							
H2Optimus-11	<u>49.3</u>	<u>47.4</u>	45.1	-	45.9	47.0	46.9
H2Optimus-12							
H2Optimus-12	<u>49.3</u>	<u>47.4</u>	45.1	-	45.9	47.0	46.9
H2Optimus-13							
H2Optimus-13	<u>49.3</u>	<u>47.4</u>	45.1	-	45.9	47.0	46.9
H2Optimus-14							
H2Optimus-14	<u>49.3</u>	<u>47.4</u>	45.1	-	45.9	47.0	46.9
H2Optimus-15							
H2Optimus-15	<u>49.3</u>	<u>47.4</u>	45.1	-	45.9	47.0	46.9
H2Optimus-16							
H2Optimus-16	<u>49.3</u>	<u>47.4</u>	45.1	-	45.9	47.0	46.9
H2Optimus-17							
H2Optimus-17	<u>49.3</u>	<u>47.4</u>	45.1	-	45.9	47.0	46.9
H2Optimus-18							
H2Optimus-18	<u>49.3</u>	<u>47.4</u>	45.1	-	45.9	47.0	46.9
H2Optimus-19							
H2Optimus-19	<u>49.3</u>	<u>47.4</u>	45.1	-	45.9	47.0	46.9
H2Optimus-20							
H2Optimus-20	<u>49.3</u>	<u>47.4</u>	45.1	-	45.9	47.0	46.9
H2Optimus-21							
H2Optimus-21	<u>49.3</u>	<u>47.4</u>	45.1	-	45.9	47.0	46.9
H2Optimus-22							
H2Optimus-22	<u>49.3</u>	<u>47.4</u>	45.1	-	45.9	47.0	46.9
H2Optimus-23							
H2Optimus-23	<u>49.3</u>	<u>47.4</u>	45.1	-	45.9	47.0	46.9
H2Optimus-24							
H2Optimus-24	<u>49.3</u>	<u>47.4</u>	45.1	-	45.9	47.0	46.9
H2Optimus-25							
H2Optimus-25	<u>49.3</u>	<u>47.4</u>	45.1	-	45.9	47.0	46.9
H2Optimus-26							
H2Optimus-26	<u>49.3</u>	<u>47.4</u>	45.1	-	45.9	47.0	46.9
H2Optimus-27							
H2Optimus-27	<u>49.3</u>	<u>47.4</u>	45.1	-	45.9	47.0	46.9
H2Optimus-28							
H2Optimus-28	<u>49.3</u>	<u>47.4</u>	45.1	-	45.9	47.0	46.9
H2Optimus-29							
H2Optimus-29	<u>49.3</u>	<u>47.4</u>	45.1	-	45.9	47.0	46.9
H2Optimus-30							
H2Optimus-30	<u>49.3</u>	<u>47.4</u>	45.1	-	45.9	47.0	46.9
H2Optimus-31							
H2Optimus-31	<u>49.3</u>	<u>47.4</u>	45.1	-	45.9	47.0	46.9
H2Optimus-32							
H2Optimus-32	<u>49.3</u>	<u>47.4</u>	45.1	-	45.9	47.0	46.9
H2Optimus-33							
H2Optimus-33	<u>49.3</u>	<u>47.4</u>	45.1	-	45.9	47.0	46.9
H2Optimus-34							
H2Optimus-34	<u>49.3</u>	<u>47.4</u>	45.1	-	45.9	47.0	46.9
H2Optimus-35							
H2Optimus-35	<u>49.3</u>	<u>47.4</u>	45.1	-	45.9	47.0	46.9
H2Optimus-36							
H2Optimus-36	<u>49.3</u>	<u>47.4</u>	45.1	-	45.9	47.0	46.9
H2Optimus-37							
H2Optimus-37	<u>49.3</u>	<u>47.4</u>	45.1	-	45.9	47.0	46.9
H2Optimus-38							
H2Optimus-38	<u>49.3</u>	<u>47.4</u>	45.1	-	45.9	47.0	46.9
H2Optimus-39							
H2Optimus-39	<u>49.3</u>	<u>47.4</u>	45.1	-	45.9	47.0	46.9
H2Optimus-40							
H2Optimus-40	<u>49.3</u>	<u>47.4</u>	45.1	-	45.9	47.0	46.9
H2Optimus-41							
H2Optimus-41	<u>49.3</u>	<u>47.4</u>	45.1	-	45.9	47.0	46.9
H2Optimus-42							
H2Optimus-42	<u>49.3</u>	<u>47.4</u>	45.1	-	45.9	47.0	46.9
H2Optimus-43							
H2Optimus-43	<u>49.3</u>	<u>47.4</u>	45.1	-	45.9	47.0	46.9
H2Optimus-44							
H2Optimus-44	<u>49.3</u>	<u>47.4</u>	45.1	-	45.9	47.0	46.9
H2Optimus-45							
H2Optimus-45	<u>49.3</u>	<u>47.4</u>	45.1	-	45.9	47.0	46.9
H2Optimus-46							
H2Optimus-46	<u>49.3</u>	<u>47.4</u>	45.1	-	45.9	47.0	46.9
H2Optimus-47							
H2Optimus-47	<u>49.3</u>	<u>47.4</u>	45.1	-	45.9	47.0	46.9
H2Optimus-48							
H2Optimus-48	<u>49.3</u>	<u>47.4</u>	45.1	-	45.9	47.0	46.9
H2Optimus-49							
H2Optimus-49	<u>49.3</u>	<u>47.4</u>	45.1	-	45.9	47.0	46.9
H2Optimus-50							
H2Optimus-50	<u>49.3</u>	<u>47.4</u>	45.1	-	45.9	47.0	46.9
H2Optimus-51							
H2Optimus-51	<u>49.3</u>	<u>47.4</u>	45.1	-	45.9	47.0	46.9
H2Optimus-52							
H2Optimus-52	<u>49.3</u>	<u>47.4</u>	45.1	-	45.9	47.0	46.9
H2Optimus-53							
H2Optimus-53	<u>49.3</u>	<u>47.4</u>	45.1	-	45.9	47.0	46.9
H2Optimus-54							
H2Optimus-54	<u>49.3</u>	<u>47.4</u>	45.1	-	45.9	47.0	46.9
H2Optimus-55							
H2Optimus-55	<u>49.3</u>	<u>47.4</u>	45.1	-	45.9	47.0	46.9
H2Optimus-56							
H2Optimus-56	<u>49.3</u>	<u>47.4</u>	45.1	-	45.9	47.0	46.9
H2Optimus-57							
H2Optimus-57	<u>49.3</u>	<u>47.4</u>	45.1	-	45.9	47.0	46.9
H2Optimus-58							
H2Optimus-58	<u>49.3</u>	<u>47.4</u>	45.1	-	45.9	47.0	46.9
H2Optimus-59							
H2Optimus-59	<u>49.3</u>	<u>47.4</u>	45.1	-	45.9	47.0	46.9
H2Optimus-60							
H2Optimus-60	<u>49.3</u>	<u>47.4</u>	45.1	-	45.9	47.0	46.9
H2Optimus-61							
H2Optimus-61	<u>49.3</u>	<u>47.4</u>	45.1	-	45.9	47.0	46.9
H2Optimus-62							
H2Optimus-62	<u>49.3</u>	<u>47.4</u>	45.1	-	45.9	47.0	46.9
H2Optimus-63							

*Results for Pluto-4G, Pluto-4S-8 and Pluto-4S-16 taken from [60]. Results for H-Optimus-1 taken from [8]. Results for H-Optimus-1 taken from [22]. Results for H-Optimus-1 taken from [63]. (Psimbench) and [30] (HEST).

Table 7: Same table content and formatting as in Table 6, but for the CLS token instead of CLS+MEAN.